Measurement of the ^{4}He 2^3P Fine Structure

A thesis presented

by

Jesse Wen

to

The Department of Physics

in partial fulfillment of the requirements

for the degree of

Doctor of Philosophy

in the subject of

Physics

Harvard University

Cambridge, Massachusetts

January 1996

Abstract

A new measurement of the 2^3P fine structure in ^{4}He is presented. The 2^3P intervals were observed by laser saturated absorption of the 1083 nm 2^3S_1–$2^3P_{0,1,2}$ transitions within a radio-frequency discharge cell. Heterodyne techniques were employed to measure optical frequencies with respect to a laser reference oscillator stabilized to the ^{3}He $2^3S_{1,F=1/2}$–$2^3P_{0,F=1/2}$ transition. The final results are $v(2^3P_0$–$2^3P_1) = 29616.936(8)$ MHz, $v(2^3P_0$–$2^3P_2) = 31908.134(8)$ MHz, and $v(2^3P_1$–$2^3P_2) = 2291.198(8)$ MHz.

Acknowledgments

Much of what I accomplished in graduate school would not have been possible without the initiative of my late advisor Frank Pipkin. Frank helped me come to Harvard, took me into his research group, and demonstrated to us all what it meant to be a gentleman and a scholar. Instead of a prolonged litany, I will simply say that it is impossible to imagine a better mentor than Frank. I have sorely missed his diligent expertise, generosity, and kindness.

Cos Papaliolios has been a trusted friend and advisor to all of Frank's remaining students and I was no exception. Cos' sound judgment, clear sense of perspective, and good humor were invaluable in guiding me through the more difficult times.

I thank Jerry Gabrielse for taking over as my official thesis advisor. Besides providing space in his lab when I was forced to move my experiment from the basement of Lyman, Jerry worked to insure that I could acquire the resources necessary to complete my work.

My graduate-school existence has benefited tremendously from the company and friendship of some of my fellow students. Ed Hagley, my partner in crime, is a constant source of surprise and inspiration. Ed enlivened the character of the entire Pipkin group; I will not soon forget our many adventures. Martin Poitzsch, another of the Pipkin clan, contributed to a lot of interesting conversations and provided much useful advice and assistance during my earlier years at Harvard. Eric Meyer has also been a

Contents

List of Figures

List of Tables

Chapter 1

Introduction

The 2^3P intervals of ^{4}He serve as an important test for atomic quantum-electrodynamic (QED) calculations and may eventually provide an improved value for the fine-structure constant α. Although the fundamental importance of this system has been recognized for some time [1], advances in computational techniques and the availability of new laser sources have recently produced substantial progress in theory and experiment. These new methods would appear to promise even more dramatic progress in the near future, perhaps permitting a detailed understanding of the helium atom with a completeness now achievable only with one-electron hydrogenic systems. In many respects, the helium 2^3P splittings are analogous to the $2p_{1/2}$–$2p_{3/2}$ fine structure in hydrogen. In both atoms, the intervals arise primarily from relativistic spin-orbit coupling and thus have an α^2 dependence to leading order. From the viewpoint of theory, the helium splittings are, of course, more difficult to calculate accurately. However, the helium levels offer considerable advantages for precise measurements: they are more than sixty times longer lived (100 ns for helium versus 1.6 ns for hydrogen) and the fine structure interval is three time larger (30 GHz versus 10 GHz). These factors

1

give helium a large intrinsic advantage and provide strong impetus for its use in a determination of α.

1.1 The Fine-Structure Constant

Since a more accurate value of α is a primary motivation, it is perhaps useful to summarize the current state of fine-structure constant determinations. A more extensive review with references is given by Taylor [2]. Presently the best values for α are:

$$\alpha^{-1}(g\text{-}2) = 137.035\ 992\ 22\ (94)\ (6.9\ \text{ppb}),$$

$$\alpha^{-1}(\text{qHe}) = 137.035\ 997\ 9\ (32)\ (24\ \text{ppb}),\ \text{and}$$

$$\alpha^{-1}(\gamma_p') = 137.035\ 984\ 0\ (51)\ (37\ \text{ppb}),$$

$$\alpha^{-1}(h/m_n) = 137.036\ 010\ 82\ (524)\ (39\ \text{ppb}),$$

where the first value is derived from the electron anomalous magnetic moment [3] and QED [4], the next from the quantum Hall effect, and the third from the proton gyromagnetic ratio determined by the so-called "low field method" and employing the adopted values for the Josephson and von Klitzing constants. $\alpha^{-1}(h/m_n)$ comes from a recent result [5] for the ratio of the Planck constant to the neutron mass. The values are depicted graphically in Figure 1.1 together with $\alpha^{-1}(\nu_{mhfs})$, which is based on a measurement of the ground-state hyperfine structure of muonium. It would seem that the agreement between the more accurate determinations of α is rather unsatisfactory with $\alpha^{-1}(\text{qHe})$ and $\alpha^{-1}(\gamma_p')$ differing by more than twice the standard deviation of their difference and with neither in close agreement with $\alpha^{-1}(g\text{-}2)$ or $\alpha^{-1}(h/m_n)$. Also, it should be noted that the $\alpha^{-1}(\text{qHe})$ and $\alpha^{-1}(\gamma_p')$
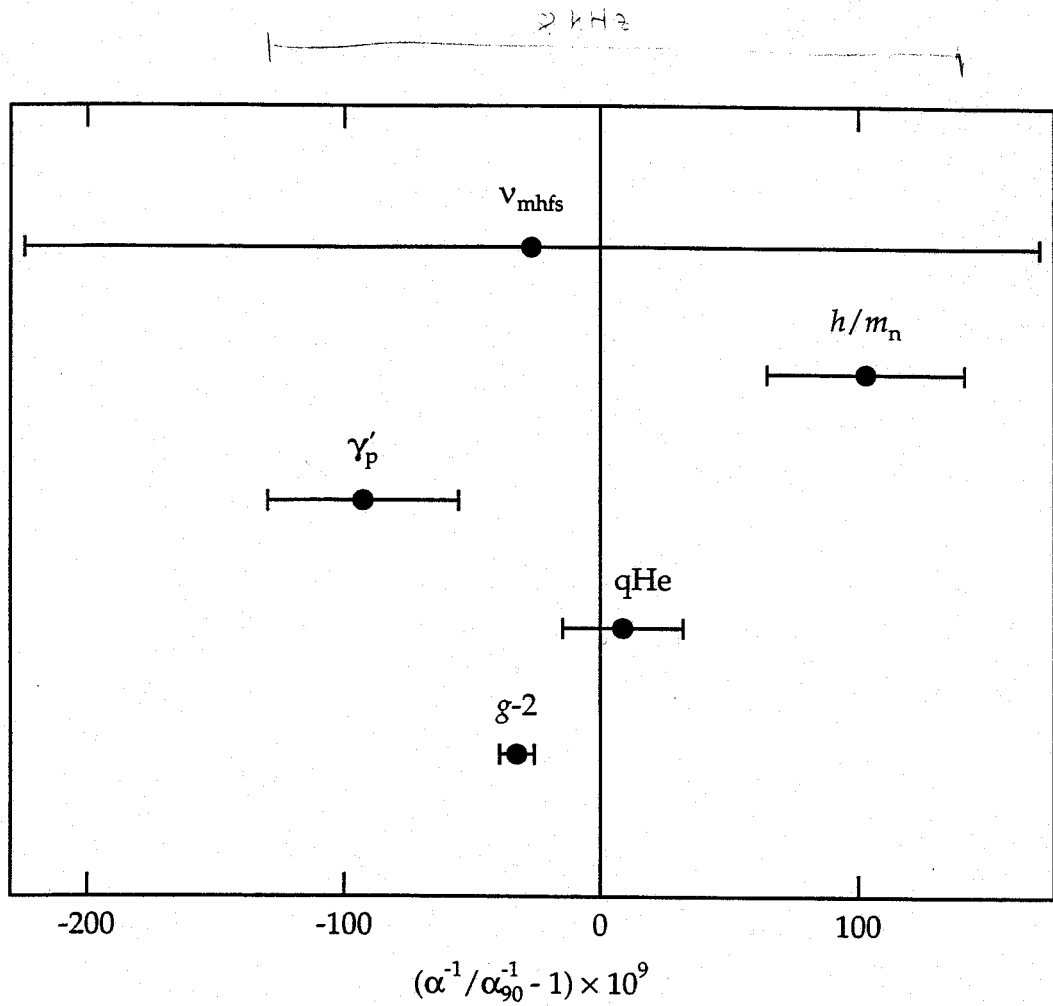
Figure 1.1. Measurements of α^{-1} plotted with respect to $\alpha_{90}^{-1} \equiv 137.035\ 996\ 720$. γ_p' refers to the proton gyromagnetic ratio, qHe to the quantum Hall effect, g-2 to the electron anomalous magnetic moment, h/m_n to the ratio of the Planck constant to the neutron mass, and ν_{mhfs} to the ground-state hyperfine structure of muonium.

numbers quoted in the present discussion refer only to results obtained at the National Institute of Standards and Technology. If other, less accurate α measurements based on the quantum Hall effect and γ_p' were to be considered, even larger discrepancies of order 200 ppb would be noticeable.

The anomalous magnetic moment of the electron has been calculated to high precision from quantum electrodynamics and is expressed as a power series in α. This series is now known accurately enough to yield a theoretical value for g-2 with an error dominated by the uncertainty in independent determinations of α. By combining the theory with a Penning-trap measurement of g-2, one arrives at the above stated result for $\alpha^{-1}(g$-2$)$. In order to stringently test QED, one would thus require an independent measurement of α at or exceeding the level of $\alpha^{-1}(g$-2$)$, i.e., 6.9 ppb. Unfortunately, as seen above, recent results seem to agree at no better than the 50 ppb level.

It is perhaps surprising that no spectroscopic method for determining α has yet given a value competitive with the four listed above. The best spectroscopic measurement of α, based on the hyperfine structure in the ground state of muonium, gives a relatively large uncertainty of 160 ppb as shown in Figure 1.1. In the classic case of the n=2 hydrogen fine structure [6], the uncertainty is even greater at about 600 ppb. It is in this context that measurements based on the ^{4}He 2^3P fine structure appear particularly promising. As previously remarked, new experimental techniques are now poised to take full advantage of the narrower lines and larger splittings available in helium while theoretical work appears capable of matching the accuracy of experiments. A measurement of the 30 GHz helium fine structure at the 1 kHz level would then give α to 16 ppb, enough to distinguish between $\alpha^{-1}(q$He$)$, $\alpha^{-1}(\gamma_p')$, and $\alpha^{-1}(h/m_n)$. A 300 Hz measurement would yield a 5 ppb value for α, which by comparison with $\alpha^{-1}(g$-2$)$ would test QED at an unprecedented level. It has been noted [7] that the helium fine structure is to lowest order a non-QED effect and thus is less dependent than g-2 on high-order QED corrections by a factor of α^{-1}. Furthermore, a

4

spectroscopic approach to measuring α, based on a simple, unambiguous atomic system, could be free of errors [8] possibly present in the bulk samples employed for determining $\alpha^{-1}(qHe)$ and $\alpha^{-1}(\gamma'_p)$. Such an atomic measurement of α could then test the condensed-matter theory of the Josephson and quantum Hall effects.

1.2 Theory of the Helium Fine Structure

Calculation of the helium fine structure involves first obtaining the spin-dependent operators which contribute to the splitting and then evaluating their contribution to the level energies by perturbation theory. The dominant effect is due to the Breit interaction [1], which arises from an approximate two-electron generalization of the Dirac equation. The first-order expectation value of this operator accounts for the inverted fine-structure of helium. In order to achieve the requisite accuracy, it is necessary to compute the Breit interaction to second order. Next, operators representing higher order QED contributions are derived from the covariant Bethe-Salpeter equation [1]. In this case, it is only necessary to take the expectation values and calculate to first order in the perturbation expansion. Finally, terms representing the effects of finite nuclear mass and mass polarization are computed.

A precise calculation is thus primarily dependent on extracting operators for the QED contributions and computing the perturbation expansion with wavefunctions of sufficient accuracy. Corrections from the Bethe-Salpeter equation to order α^4 (in atomic units) were first derived by Douglas and Kroll [9] as a sum of sixteen spin-dependent operators.

5

Evaluation of the perturbation series by a number of workers [10, 11] then culminated in the results of Lewis and Serafino [12]. At this point, a theoretical uncertainty of roughly 1 ppm was claimed, still far short of that now required for a competitive α measurement. However, a major advance over the previous results has recently been achieved by Yan and Drake [7]. By constructing extremely accurate variational wavefunctions from augmented Hylleraas basis sets, they were able to achieve convergence at the 3 ppb level in their computation of all terms through order α^4. Employing a more rigorous treatment of QED corrections, Zhang and Drake [13] have verified the completeness of the Douglas-Kroll terms to order α^4 and laid the groundwork for the derivation of higher order corrections. In fact, the contribution from the $\alpha^5 \ln \alpha$ term has now been calculated [14] and is included in the theoretical value reported in Table 4.1. As discussed in Chapter 4, the evaluation of higher-order terms, which presently dominate the theoretical uncertainty, could result in a sub-kilohertz calculation in the foreseeable future.

1.3 Previous Measurements

Early experiments on the 2^3P splittings were undertaken with both microwave [15] and optical techniques [16], including the method of level crossing [17]. The first measurement to claim an uncertainty at the 1 ppm level came from the work of Hughes and coworkers [18-22]. They employed a helium beam excited by electron bombardment to produce atoms in the metastable 2^3S_1 state. The three magnetic sublevels, m = 0, ±1, were spatially separated by deflection magnets so the population in each sublevel could be

monitored via a moveable detector. Within an interaction region, light from a helium discharge populated the 2^3P levels while microwave radiation drove transitions between the fine-structure levels. The transitions were tuned by varying a uniform magnetic field surrounding the interaction region. Following this region, the 2^3P population would decay to the 2^3S_1 state, resulting in a redistribution of atoms between the $m = 0, \pm 1$ sublevels. By detecting this change in population while varying the magnetic field of the interaction-region, resonance line shapes were obtained giving the transition frequencies of the 2^3P fine structure. In the end, these experiments were limited by beam counting statistics. An improved measurement thus requires better excitation or detection efficiency.

A substantial improvement can be obtained by laser excitation of the 2^3P levels from the metastable 2^3S_1 state. The fine structure could then be directly resolved by laser spectroscopy. The optical 2^3S_1–2^3P transitions, with saturation intensities of a fraction of a mW/cm^2, are much stronger than the magnetic-dipole microwave transitions mentioned above. In addition to the greatly increased excitation efficiency this implies, laser detection methods can be applied to enhance the detection sensitivity. Finally, the 1.6 MHz natural width of the optical 2^3S_1–2^3P transitions is half that of the microwave transitions between 2^3P levels since the lower 2^3S_1 state is metastable. Until recently, such gains were unrealized due to the difficulty of obtaining laser radiation at the 2^3S_1–2^3P wavelength of 1083 nm. The discovery of hexagonal lanthanum neodymium hexa-aluminate $La_{1-x}Nd_xMgAl_{11}O_{19}$ (LNA), a material capable of lasing at 1083 nm, facilitated the construction of the required lasers [23]. A number of experiments [24, 25] on the 2^3S_1–2^3P transitions quickly followed, including a measurement of the 2^3P fine structure by Shiner *et al.* [26, 27]. As in the experiments of Hughes and

coworkers, this measurement also employed spatial deflection of a polarized metastable-helium beam as a means of detection, the main difference being that the optical-microwave magnetic resonance was replaced by laser excitation to the 2^3P levels. As before, subsequent decay back to the 2^3S_1 state produced a change in polarization which was detected. Line centers were found by varying the laser wavelength, which was measured by comparison to an iodine-stabilized He-Ne laser via a Fabry-Perot interferometer. Taking the difference between optical transition frequencies derived from wavelength measurements yielded each of the fine-structure splittings. Initially an uncertainty of 9 kHz was assigned [26] but this was subsequently reduced to 3 kHz with essentially no other change to the measured values [27]. The results, as given in Table 4.1 and Figure 4.1, were not in good agreement with those arrived at by Hughes and coworkers and clearly needed verification. In particular, the method of measuring the laser frequencies, by wavelength comparisons with a Fabry-Perot interferometer, seemed especially susceptible to systematic errors. Also, beam counting statistics still required several minutes of averaging at each laser frequency to achieve the quoted accuracy. An improved measurement would require progress in both frequency metrology and signal-to-noise ratio.

1.4 Overview

This thesis describes a new experiment to measure the helium 2^3P fine structure. The technique employs laser saturated-absorption spectroscopy in helium discharge cells to achieve substantial improvements in signal-to-noise ratio over previous atomic-beam experiments. This facilitates the

accurate determination of line centers and the identification of systematic effects. The level splittings are determined by laser heterodyne methods giving frequency measurements free of the difficulties inherent in the interferometric wavelength metrology employed in past experiments. Heterodyne techniques also permit more explicit characterization of laser performance. Although the measurement uncertainty has only been demonstrated at the 8 kHz level, it is anticipated that pending modifications to the apparatus will permit an accuracy well beyond what has been achieved to date. The following chapters will detail the design and construction of the apparatus as well as methods of data collection and analysis. This will be followed by a discussion of results and possible improvements to permit an even more precise measurement.

Chapter 2

Description of Apparatus

The experiment consists essentially of two lasers together with helium absorption cells, optics, and electronics for frequency control and data acquisition. One laser, henceforth referred to as the clock laser, is stabilized to a fixed frequency and serves as a local reference oscillator. The remaining laser, known as the sweep laser, is scanned over the transitions of interest by precisely controlling its frequency offset from the clock laser. Splittings between transitions can then be accurately obtained from this offset frequency, without the need for measurement of the absolute clock or sweep laser frequencies.

The helium levels relevant to the present work are depicted in Figure 2.1. The clock laser is stabilized by locking its frequency to that of the ^{3}He $2^3S_{1,F=1/2}$–$2^3P_{0,F=1/2}$ transition. As described in more detail below, this frequency servo is realized by employing fm spectroscopy on a ^{3}He discharge cell. The frequency difference between the clock and sweep lasers is obtained by mixing their beams on a high speed photodiode. This heterodyne signal is then held at a precisely controlled frequency by a phase-locked loop which drives the frequency of the sweep laser. By varying the difference frequency
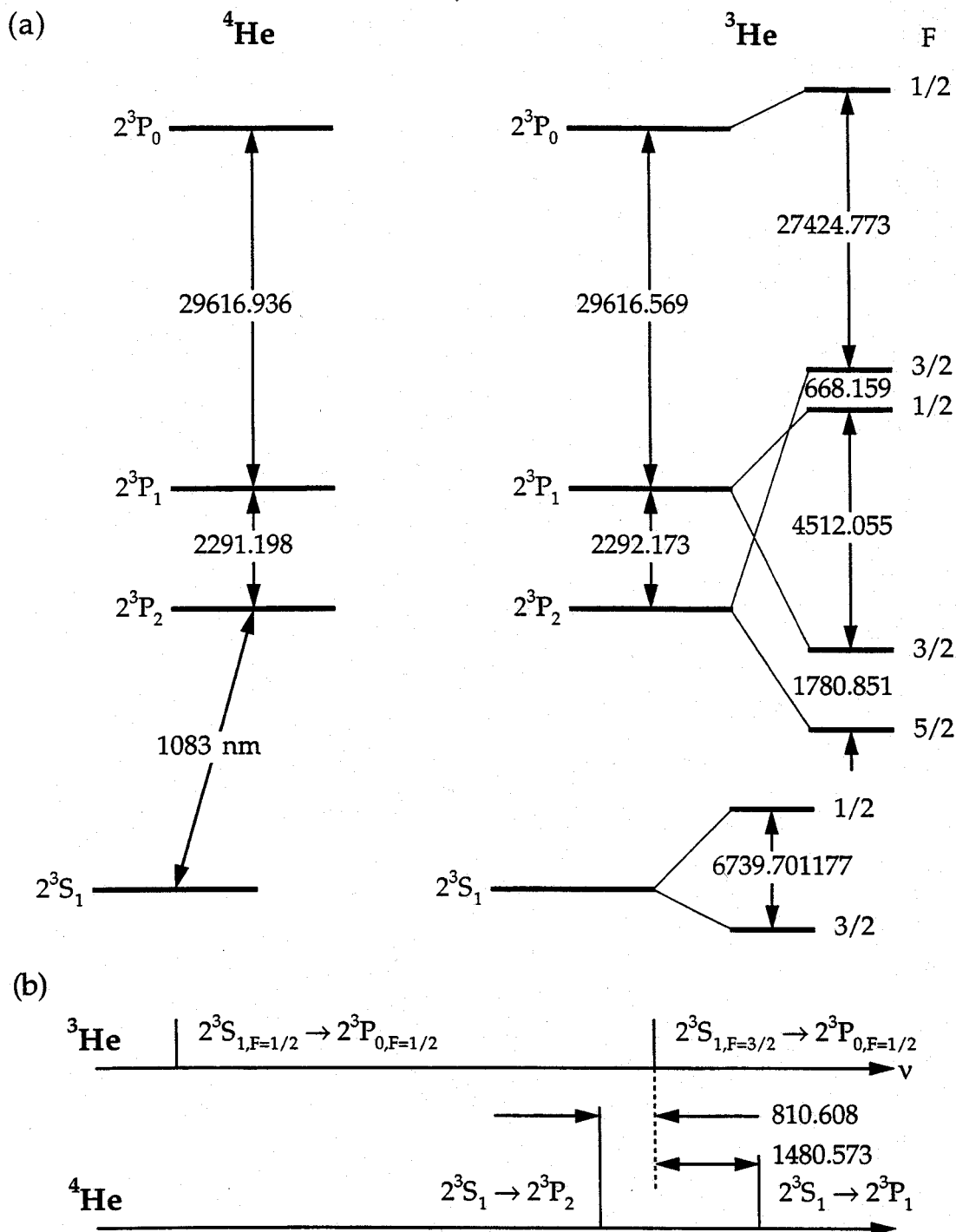
Figure 2.1. (a) Energy levels for ^{3}He (shown both with and without the hyperfine interaction [24, 28]) and ^{4}He. (b) Relative positions of transitions for the two isotopes. All intervals in MHz unless otherwise indicated.

under computer control, the sweep laser is made to scan the ^{4}He 2^3S_1–$2^3P_{0,1,2}$ transitions, which are observed by saturated absorption in a second discharge cell containing only ^{4}He. The fine-structure splittings are then obtained as the intervals between the observed line centers.

The remainder of this chapter details the design and construction of the various parts of the experiment. Figure 2.2 is a simplified block diagram showing the two lasers, their respective helium spectroscopy setups, and the frequency-offset locking apparatus. The discussion below first concentrates on the lasers, then examines saturated absorption and fm spectroscopy, and concludes with a description of the frequency-offset lock.

2.1 Lasers

The clock and sweep lasers are nearly identical in design. Each consists of a standing-wave resonator containing an LNA rod which is end-pumped by a laser-diode array. A similar laser has been reported by Chuang and Metcalf [29]. Figure 2.3 shows the construction of the lasers built for the present measurement. These lasers represent a departure from previous LNA lasers assembled in our laboratory in that the earlier devices were argon-ion-laser pumped ring oscillators. It was felt that the simpler, more compact standing-wave cavity would permit a greater degree of mechanical rigidity and also be more immune from thermally induced frequency hops (see below). In addition, laser-diode pumping provides more reliability and amplitude stability than is possible with argon-ion lasers. The power available from the standing-wave lasers is much less than that obtained in
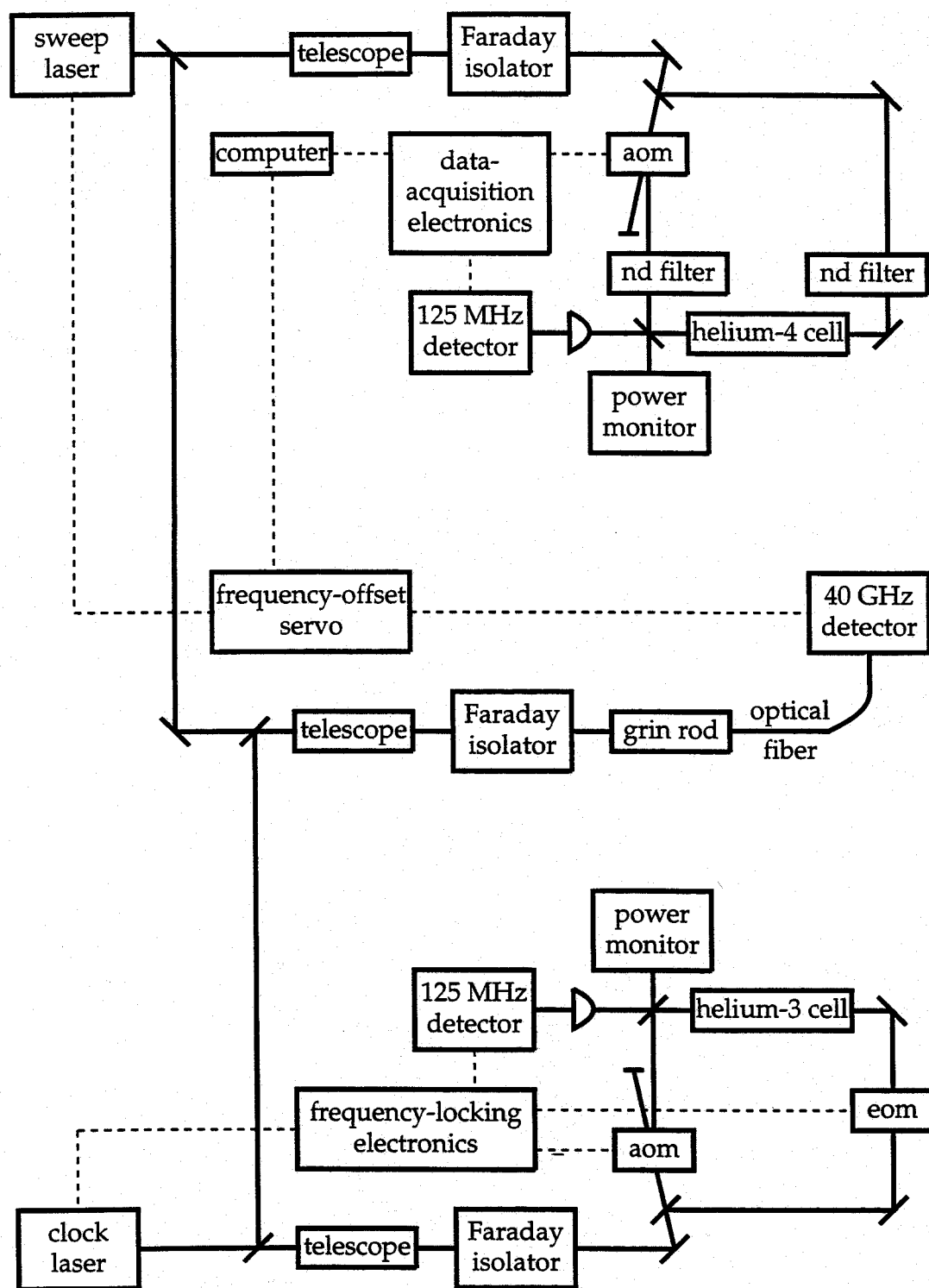
Figure 2.2. Simplified diagram of the experiment.

13

the past from the ring lasers but is sufficient for the purposes of this experiment.

2.1.1 Laser-Diode Pumping

The laser-diode arrays (SDL-2372-P1) used for pumping are capable of emitting up to 2 W in a wavelength range around 795 nm. The array itself forms an effective 200 μm $\times$ 1 μm output aperture and produces a far-field radiation pattern with an approximately 3:1 aspect ratio. The diode assembly also includes a thermoelectric cooler (tec), temperature-sensing thermistor, and monitor photodiode. The entire package is connected to an ILX Lightwave LDC-3752 laser-diode controller which provides current and temperature regulation to the diode array as well as read-out circuitry for the monitor photodiode. Typically, the current is set at 2 A, resulting in 1.1 W of optical power. The temperature is set to shift the wavelength so it coincides with the 795 nm absorption maximum [30] of LNA. Initially, the temperature dependence of the wavelength was calibrated with a commercial wavemeter. However, as the diode aged, small temperature adjustments were necessary to maintain peak output power from the LNA resonator. Both arrays were specified to run with a wavelength of 795 nm at or somewhat below 25° C.

The highly divergent (32° fwhm perpendicular to the junction, 12° parallel) output of the array is collimated by a four-element lens (Special Optics model 54-18-15). This lens has an effective focal length of 15 mm and a conveniently large back working distance of 4.2 mm from the laser output facet to the housing face. Its numerical aperture of 0.6 provides high
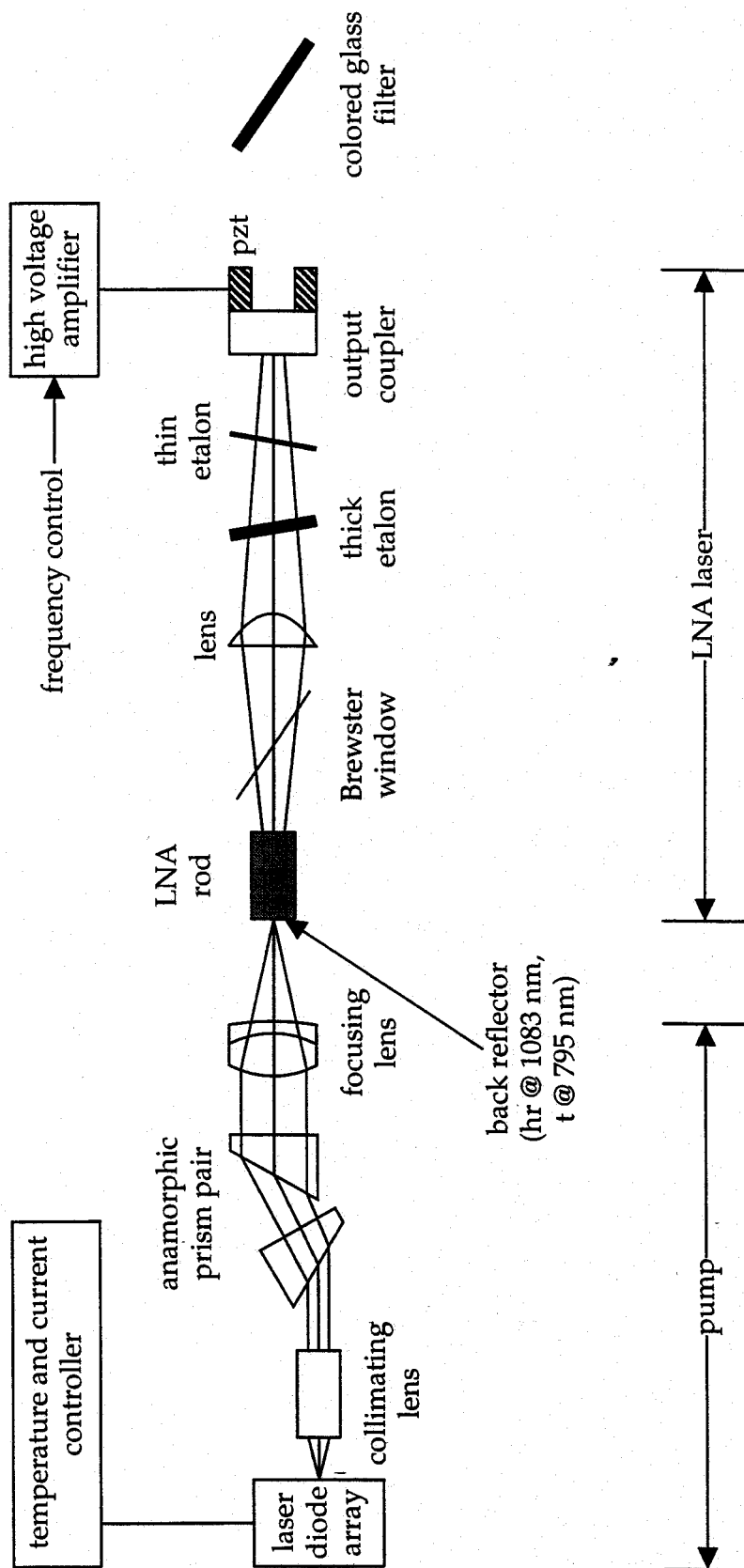
Figure 2.3. Diode pump assembly and LNA laser.

collection efficiency while its diffraction-limited performance over a 1° field of view is more than sufficient for the 200 μm stripe of the array.

Following the collimating objective, the beam is made symmetric by expanding along its smaller dimension with a 3× anamorphic prism pair, thus correcting for the approximate 3:1 aspect ratio. Finally, a cemented doublet lens with a 35 mm focal length focuses the pump beam into the LNA gain medium. In essence, the pump optics (collimating lens, anamorphic prism, and focusing lens) serve to image the 200 μm × 1 μm output aperture of the array on to the LNA rod with a demagnification of 0.778 (35 mm ÷ 15 mm ÷ 3) parallel to the diode junction and a magnification of 2.33 (35 mm ÷ 15 mm) perpendicular to it. The resulting image is thus 156 μm × 2.33 μm. The focal length of the focusing lens is chosen to produce a spot size and divergence which give efficient pumping of the TEM_{00} mode of the resonator while avoiding excitation of higher order modes. In practice, the focal length was determined by trying a series of lenses and choosing the one which resulted in the highest output power while maintaining a TEM_{00} mode structure.

2.1.2 LNA Laser

The cavity of the LNA laser itself is constructed in a linear standing-wave configuration enclosed by the high reflection(hr)-coated end of the LNA rod at one end and the output coupler at the other. An antireflection(ar)-coated singlet lens with a 40 mm focal length is placed within the cavity roughly 55 mm from the hr end of the rod. This lens position is chosen to produce a beam waist at the LNA-rod end of the cavity which matches the

incoming pump beam. In practice, the lens position is varied until a clean TEM_{00} mode is observed at the output. Both ends of the resonator are optically flat and thus the Gaussian cavity modes have their maximum diameter at the lens and their waists at each end of the cavity. The spot size at each waist can be calculated by standard methods of Gaussian optics and are given by

$$w_1^2 = \frac{\lambda l_0}{\pi} \left[\frac{g_2}{g_1(1 - g_1 g_2)} \right]^{1/2}, \tag{2.1}$$

$$w_2^2 = \frac{g_1}{g_2} w_1^2, \tag{2.2}$$

where w_1 and w_2 refer to the waist at the rod and output coupler respectively. Also,

$$l_0 = \frac{d}{n} + l_1 + l_2 - \left(\frac{d}{n} + l_1 \right) \frac{l_2}{f}, \tag{2.3}$$

$$g_1 = 1 - \frac{l_2}{f}, \tag{2.4}$$

$$g_2 = 1 - \frac{\frac{d}{n} + l_1}{f}, \tag{2.5}$$

where d and n are the length and index of refraction respectively of the LNA rod, l_1 is the distance between the rod and the lens, and l_2 is the distance from the lens to the output coupler. Strictly speaking, these results apply only in the case of a passive cavity formed by just the end mirrors, the lens, and an unpumped LNA rod. Effects due to the active gain medium and additional intracavity elements (e.g., etalons) have been neglected and often lead to distortions of the mode structure. Thus, during actual construction of the

laser, placement of the optical elements by trial and error is invariably necessary to achieve optimum results.

The LNA material was obtained from Union Carbide in the form of a 4-mm-diameter cylinder whose axis is parallel to the crystalline c-axis. This orientation has been reported [23] to give the best laser efficiency. The crystal was doped with a Nd concentration of 15% and has an index of refraction of 1.75 at the 1083 nm wavelength. The ends of the rod were polished and coated by Virgo Optics to give a length of 8.5 mm. The face capping one end of the laser cavity is polished flat and perpendicular to the rod axis and has a coating which permits transmission (> 90% t) of the 795 nm pump radiation while maintaining high reflectivity (> 99.5% r) at 1083 nm. The other end of the crystal, which resides within the resonator, is polished flat with a small 15' wedge angle to direct reflections out of the cavity. In addition, the surface is ar coated for 1083 nm. The rod is held snugly in a split copper ring which seems to provide an adequate degree of heat sinking.

The overall optical length of the cavity is approximately 190 mm, thus giving a frequency spacing of roughly 800 MHz between adjacent longitudinal modes. Substitution of the resonator dimensions into Equations (2.1)–(2.5) leads to a spot size (full Gaussian width) of $2w_1 = 110 \, \mu m$ at the waist within the LNA rod. This is a reasonably close match to the 156 μm spot size of the pump beam although the somewhat larger pump waist implies that careful centering of the pump beam is required to force lasing in only the TEM_{00} mode. It is found in practice that this is indeed the case and that, as would be expected, adjustment of the pump beam in the direction along the diode facet is particularly crucial since this is the largest dimension of the pump spot.

Single-frequency operation of the laser is achieved with the combination of a dichroic coating and two etalons. The fluorescence —

18

spectrum of LNA is strongest in a band at 1055 nm, which must be suppressed to allow lasing in the somewhat weaker desired band at 1083 nm. A dichroic coating on the output coupler with roughly 96% r at 1083 nm and 60% r at 1055 nm quenches oscillation on the stronger emission band. The very sharp cutoff of this coating, produced by Thin Film Labs, has a wavelength which depends on the position of the substrate in the coating chamber. Since it was difficult to predict the placement which would produce the correct cutoff between the two closely spaced wavelengths, substrates were placed at three different heights in the chamber and subsequently tested with a spectrophotometer to select the group with the best transition between 1055 nm and 1083 nm. Even with this procedure, the results are probably less than optimal. In particular, the cutoff should be shifted slightly to the red to produce more transmission at 1083 nm, perhaps 92% r, which would probably be a better level of output coupling yielding higher usable power.

A single longitudinal mode of the laser cavity is selected with the insertion of two solid fused-silica etalons. The thicker of the two etalons serves to suppress adjacent cavity modes while the thinner one insures that lasing does not occur in multiple thick-etalon modes. For each etalon, the thickness determines its free spectral range (fsr), given by

$$\text{fsr} = \frac{c}{2nl} \, , \tag{2.6}$$

where c is the speed of light, n the index of refraction (for fused silica $n = 1.45$), and l the etalon thickness. The finesse (F) of the etalon is given by

$$F = \frac{\pi\sqrt{R}}{1-R} \, , \tag{2.7}$$

where R is the power reflectivity of each surface, leading to the corresponding fringe halfwidth

$$\Delta v = \frac{\text{fsr}}{F} = \frac{c(1-R)}{2\pi n l \sqrt{R}}.$$ (2.8)

Tilting the etalon results in discontinuous tuning of the laser as different modes are selected. In choosing etalons, it is also important to consider the etalon insertion loss L, which has been shown [31] to be given by the approximate analytical expression

$$L = 8R\left[\frac{l\theta}{nw(1-R)}\right]^2,$$ (2.9)

where θ is the tilt angle of the etalon and w the beam waist at the etalon.

In each laser, the thick etalon was selected so that its thickness gave a fsr large enough to preclude lasing at more than one fringe and also so that its reflectivity per surface gave a fringe width narrow enough to discriminate against adjacent cavity modes. Etalon selection was complicated by the roughly 2800 GHz width [32] of the LNA gain curve which thereby required the use of relatively thin etalons. Due to the large fsr of such etalons, fairly high reflectivities were needed to achieve sufficiently narrow fringe widths. Unfortunately, it was found that such etalons could not be angle tuned through an entire fsr without incurring unacceptable insertion loss. It was thus necessary to individually test etalons and select those whose fringes were near the helium lines of interest and thereby did not require large tilt angles. After trying a number of etalons, only two were found to permit tuning to the

helium lines with acceptable laser power. One was 150 μm thick with 65% r on each surface and was inserted into the sweep laser while the other, placed in the clock laser, was 200 μm thick with also 65% r per surface.

From Equations (2.6) and (2.8), the 150 μm etalon has a fsr of 689 GHz and a fringe half width of 95 GHz. For the 200 μm etalon, the corresponding values are 517 GHz and 71 GHz. It is somewhat surprising that such large fringe widths can suppress cavity modes separated by only 800 MHz. However, spatial hole burning induced in the solid-state gain medium by the standing waves of the resonator also serves to prevent oscillation in adjacent modes. This mechanism probably accounts for the ability to achieve single-mode operation with the present etalons. It was also occasionally observed that lasing would occur at multiple thick-etalon fringes. To insure oscillation within only a single fringe and thus lend a greater degree of robustness to the laser, a second etalon with a thickness of 75 μm, corresponding to a fsr of 1378 GHz, was inserted into each laser. It was not necessary to coat this thin etalon since Fresnel reflection from the fused-silica surfaces gave a high enough finesse to quench adjacent thick-etalon modes.

Continuous tuning of the laser was obtained by mounting the output coupler on a ring-shaped piezoelectric transducer (pzt). In order to increase the mechanical resonance frequency of the transducer assembly, a relatively small 0.305" diameter × 0.125" thick substrate was chosen for the output coupler and the pzt itself was sandwiched between the output coupler and a stiff 2" diameter × 0.5" thick alumina disc which had a 0.25" hole bored through the center to permit passage of the output beam. The ring pzt, purchased from Morgan Matroc, consists of layers of PZT-5H ceramic interleaved with platinum electrodes, all fired together as an integral unit with an outer diameter of 0.395", inner diameter of 0.205", and thickness of

0.160". The close electrode spacing and consequent high electric fields permitted by this construction give a large displacement of 7 nm/V but also a fairly high capacitance of 60 nF. The pzt actuator is driven by a Krohn-Hite KH7602 high voltage amplifier with a bandwidth of 1 MHz and maximum output voltage of 400 V.

The laser is forced to oscillate in a fixed linear polarization by the insertion of a 1-mm-thick fused-silica Brewster-angle window. Finally, the resonator frame consists primarily of four 1" diameter × 7" long spacer bars constructed from super-invar for thermal stability. Relative immunity of the cavity to thermal contraction or expansion helps insure that the maximum pzt displacement will not be exceeded while the resonator length is servo controlled to maintain a laser frequency lock. During operation, the main difficulty is actually drift of the thick-etalon fringe position with temperature. This drift eventually results in selection of a different cavity mode and a frequency hop of the laser. It can be easily shown that the fringes of a fused-silica etalon change position with temperature at a rate of approximately 2.1 GHz/°C, independent of fsr. The compact size of the cavity, which gives a larger spacing between its modes, thus results in a longer interval between mode hops. In fact, the clock laser typically stays locked to its line without mode hops for the entire duration of a data run, usually about eight hours. Before being sent to the remainder of the experiment, the laser output is passed through a colored glass filter (Newport FSQ-RG850) which passes wavelengths longer than 850 nm to remove any possible contamination by the pump beam.

2.2 Helium Absorption Spectroscopy

The experiment is centered around two spectrometers, one for each laser, as shown in Figure 2.2. In each case, helium lines are observed in absorption through a gas discharge cell. Although previous experiments have employed metastable-helium beams, the much higher atom densities within a cell lead to a vast improvement in signal-to-noise ratio, which is critical in the frequency locking and line splitting required to advance beyond current measurements. Furthermore, since the 1.6 MHz natural width of the 1083 nm helium lines is comparable to their collision-broadened width in a low pressure cell, the collision-free environment of a beam does not produce much additional line narrowing. In the present experiment, cell line widths of 6.5 MHz have been observed and it may be possible to reduce this further by, for example, cooling the cell with cryogenic techniques. The main concern then is with possible systematic shifts in the lines from the cell environment. The helium lines at 1083 nm have been observed to exhibit a fractional pressure shift of about -3.6 ppb/Torr [24]. If such a fractional shift were to persist for the 2^3P intervals, it would pose no difficulties even at our measurement goal of 10 ppb since the cell pressure is typically only 50 mTorr. Beyond this speculation, it is difficult to predict the actual magnitude of possible shifts at this level. However, it should be noted that a past microwave measurement [33] on the ^{3}He $2^3S_{1,F=1/2}$–$2^3S_{0,F=3/2}$ hyperfine structure in a discharge cell achieved an uncertainty of 2.4 ppb and observed a fractional pressure shift for this hyperfine interval of 7.4 ± 3.0 ppb/Torr. It is thus not unreasonable to hope for similar shifts in the ^{4}He 2^3P fine structure.

2.2.1 Saturated Absorption Spectroscopy with the Sweep Laser

The ^{4}He 2^3S_1–$2^3P_{0,1,2}$ optical transitions are observed by saturated absorption spectroscopy in order to obtain sub-Doppler line widths. The output of the sweep laser is first sent through a Galilean telescope with a 4:1 demagnification. This telescope provides control over beam collimation and also gives the smaller beam diameter required to clear device apertures further down the line. A Faraday isolator (Optics for Research model IO-D-1083) immediately follows the telescope and provides 30–40 dB of isolation. Without this isolator, spurious fluctuations were observed in the helium absorption signal. The beam fits easily within the 1.5 mm apertures of the isolator although it is slightly expanding at this point. Since the Faraday effect results in a rotation of the beam's linear polarization by 45°, a half-wave plate is inserted at the isolator output to restore the original polarization state.

The pump and probe beams required for saturated absorption are formed by splitting the beam after the half-wave plate with the uncoated surface of an optically flat piece of BK-7 glass. The beamsplitter is oriented to give a 45° angle of incidence thus resulting in a Fresnel reflection coefficient of about 10%. The reflected portion of the beam becomes the probe while the remainder is the pump. The 0.25" thickness of the beamsplitter and an ar coating on its second surface serve to minimize the effects of ghosting.

An acousto-optic modulator (aom) (Isomet model 1205C-2) is introduced into the pump beam in order to chop its amplitude for purposes of synchronous detection and to shift the pump frequency with respect to the probe. As shown in Figure 2.4, which depicts the helium-spectrometer

24
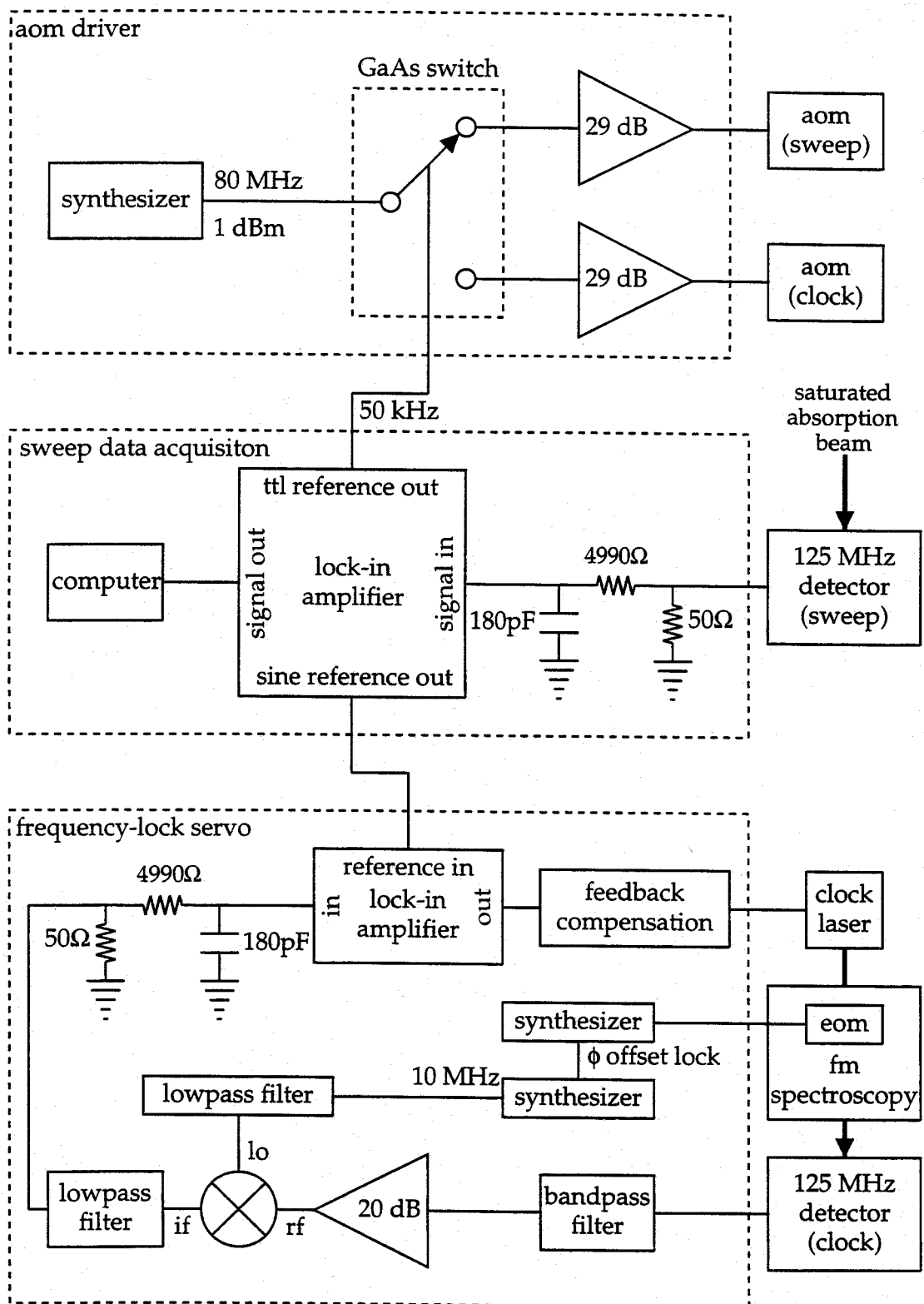
Figure 2.4. Electronics for acquiring absorption signals and frequency locking.

electronics for both lasers, the rf drive signal for the aom originates from an HP8647A synthesizer which is set to produce an 80 MHz sine wave at a power level of 1 dBm. The synthesizer output is then chopped by a spdt GaAs switch controlled by the ttl-level reference output of a lock-in amplifier. This lock-in is employed for signal detection as detailed below and is set to produce a 50 kHz reference signal. Each switch output is then fed to a 2 W power amplifier (Mini-Circuits model ZHL-1-2W) with a gain of roughly 29 dB thereby resulting in approximately 1 W of rf power. One of the amplifiers drives the sweep-laser aom while the other drives an analogous aom within the clock-laser setup. The aom is angled to maximize the power in the first-order frequency-up-shifted beam while the zeroth-order beam is blocked by a beam stop. A diffraction efficiency of about 70% was measured and, since this is more than sufficient for the present purposes, no further attempt at improvement was made. The resulting pump beam is thus shifted up in frequency by 80 MHz with respect to the probe and is 100% amplitude modulated with a 50 kHz square-wave envelope.

The pump and probe beams are made to counterpropagate through the ^{4}He discharge cell in a standard saturated-absorption configuration. As is well known, a hole burned by the pump beam in the atomic velocity distribution within the cell is detected by the probe, thus resulting in a narrow sub-Doppler line shape. Since the pump frequency is 80 MHz above that of the probe, the atomic velocity group which resonates simultaneously with both beams will not be at rest but rather will sit on one side of the distribution. In fact, as seen by the probe beam, the center of the narrow saturated-absorption line is below the peak of the Doppler profile by 40 MHz, half the pump-probe frequency difference. The pump-probe frequency offset eliminates the possibility that light scattered from the pump into the probe channel will

produce optical-interference artifacts in the detected line shape since any such effects would have a characteristic frequency of 80 MHz, well above the detection bandwidth.

After passing through the cell, the probe beam is separated from the pump by transmission through a 25% r beamsplitter and then focused on an InGaAs photoreceiver (New Focus model 1811) with an rf bandwidth of 125 MHz and a maximum conversion gain of 32 V/mW. The beamsplitter also reflects the pump beam into the cell resulting in a factor of four pump attenuation. In the vicinity of the cell, both beams have a diameter of roughly 5 mm and a neutral density filter is inserted in each beam to control its intensity. Generally, the pump/probe power ratio is maintained at approximately 1.7. The output of the photoreceiver is terminated in 50 Ω and then goes through a 177 kHz low-pass rc filter before entering a digital lock-in amplifier (Stanford model SR830). The low-pass filter serves to remove any high frequency components which might pose a difficulty for the active filters in the lock-in. The lock-in reference provides the 50 kHz aom chop signal described above and the lock-in is thus set to detect probe beam signals synchronized with the pump amplitude modulation. This isolates the narrow, pump-induced saturated-absorption line from the Doppler-broadened profile seen by the probe alone. The lock-in output is then read by computer as the sweep laser traverses the helium transitions giving the line shapes shown in the next chapter. In addition, the sweep laser power is monitored by measuring with a silicon photodiode the intensity of the portion of the pump transmitted by the 25% r beamsplitter. The photodiode has a 1 cm × 1 cm active area coated with a resin which passes wavelengths longer than 840 nm to screen out background light. The current from this photodiode is shunted through 50 Ω and the resulting voltage read by a

second digital lock-in amplifier phase-locked to the aom chop reference. Figure 2.5 shows a calibration curve relating lock-in output reading to pump power incident on the discharge cell.
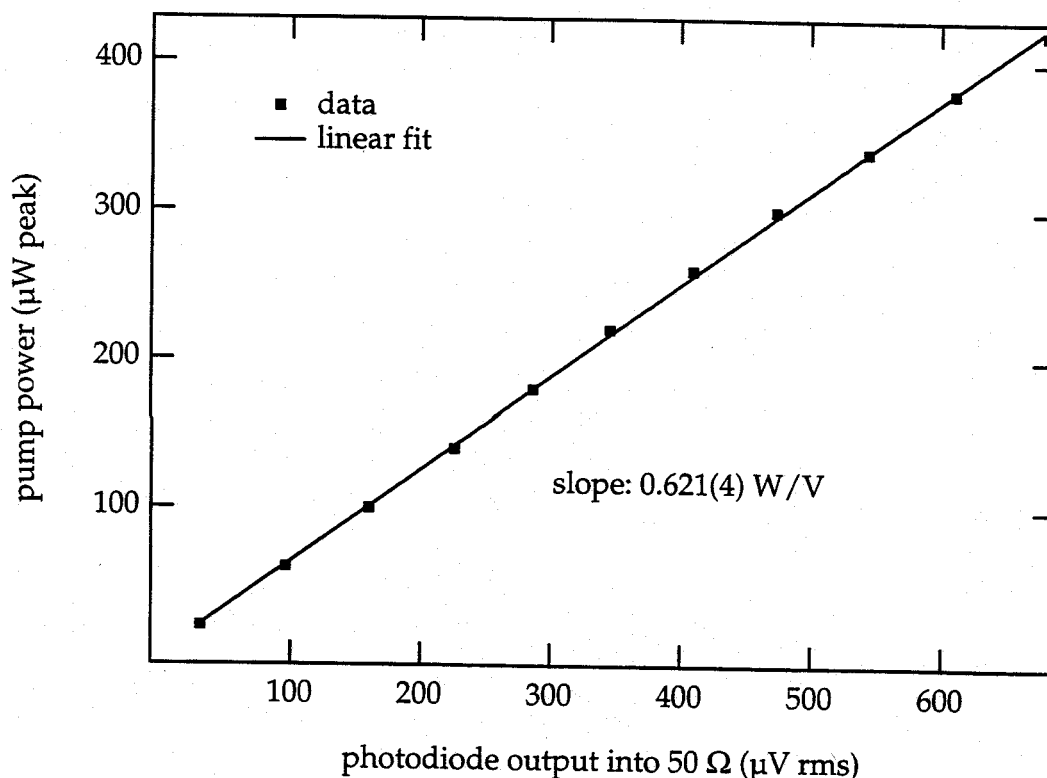
Figure 2.5. Calibration curve for sweep-laser power-monitor photodiode.

All the helium cells employed in the experiment were fabricated, by Opthos Instruments, entirely of Pyrex by optically contacting windows to the ends of a section of 25 mm diameter tubing. Three ^{4}He cells with lengths of 150 mm, 125 mm, and 100 mm were filled to pressures of 50 mTorr, 100 mTorr, and 200 mTorr respectively. The longer cell lengths were meant to compensate for reduced absorption at the lower pressures. Data were taken

with each cell to investigate the effects of varying the pressure. Population in the 2^3S_1 metastable state was generated by maintaining an rf discharge within the cell. The discharge was driven by the Colpitts oscillator circuit shown in Figure 2.6. The circuit is virtually identical to one [34] previously used in our laboratory. Rf power was coupled into the cell via an inductor consisting of eight turns of twelve-gauge copper wire circling the cell for a length of roughly 2". The tank circuit formed with this inductor gives a discharge oscillation frequency near 50 MHz. The strength of the discharge was adjusted by varying the dc supply voltage to the Colpitts oscillator.
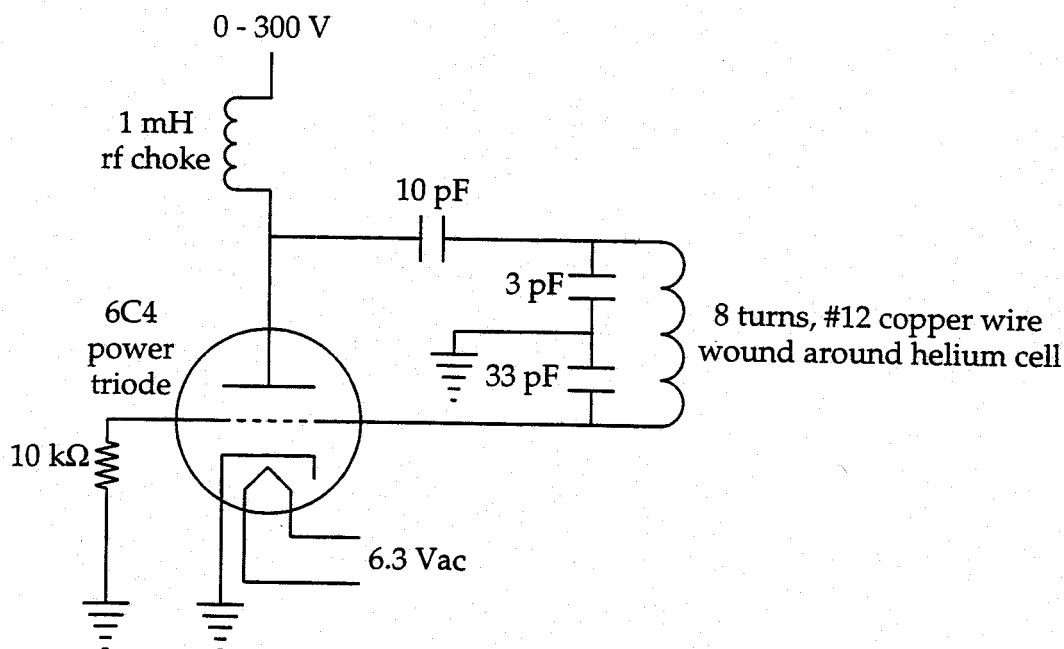
Figure 2.6. Colpitts oscillator circuit for producing the rf discharge.

In order to provide some degree of magnetic shielding, the cell and inductor are enclosed in a 2" diameter × 10" long mu-metal cylinder formed

from 0.025" thick sheet material. A Teflon spacer serves to center the cell within the shield and to insulate the inductor from the mu-metal. It was found that the leads to the inductor have to be less than about 3" to 4" in length for the discharge circuit to work properly and thus a 0.25" wide slot was cut along the length of the mu-metal shield to permit insertion of the inductor leads by the shortest possible path. Despite the presence of this slot, *in situ* measurements with a magnetometer and a Hall probe found the magnetic field to be less than 50 mG in all directions at any internal point more than one diameter (2") from either end of the shield.

2.2.2 FM Spectroscopy with the Clock Laser

The spectrometer for the clock laser duplicates essentially all the elements found in the apparatus for the sweep laser and also incorporates additional components required for frequency stabilization to an atomic line. As mentioned above and shown in Figure 2.4, the clock-laser aom chop signal derives from the same reference as that for the sweep laser. The power of the clock laser is monitored in exactly the same way as for the sweep laser and the corresponding calibration curve is given in Figure 2.7.

Techniques of fm spectroscopy, which are well documented [35, 36], are used to produce a clean and accurate frequency-discriminator signal for locking to the appropriate line in a ^{3}He cell. This requires the addition of an electro-optic phase modulator (eom), as shown in Figure 2.2, and corresponding demodulation circuitry, shown in Figure 2.4. In essence, balanced phase-modulation sidebands are produced on the probe by the eom and, upon encountering the pump-induced hole in the atomic population,
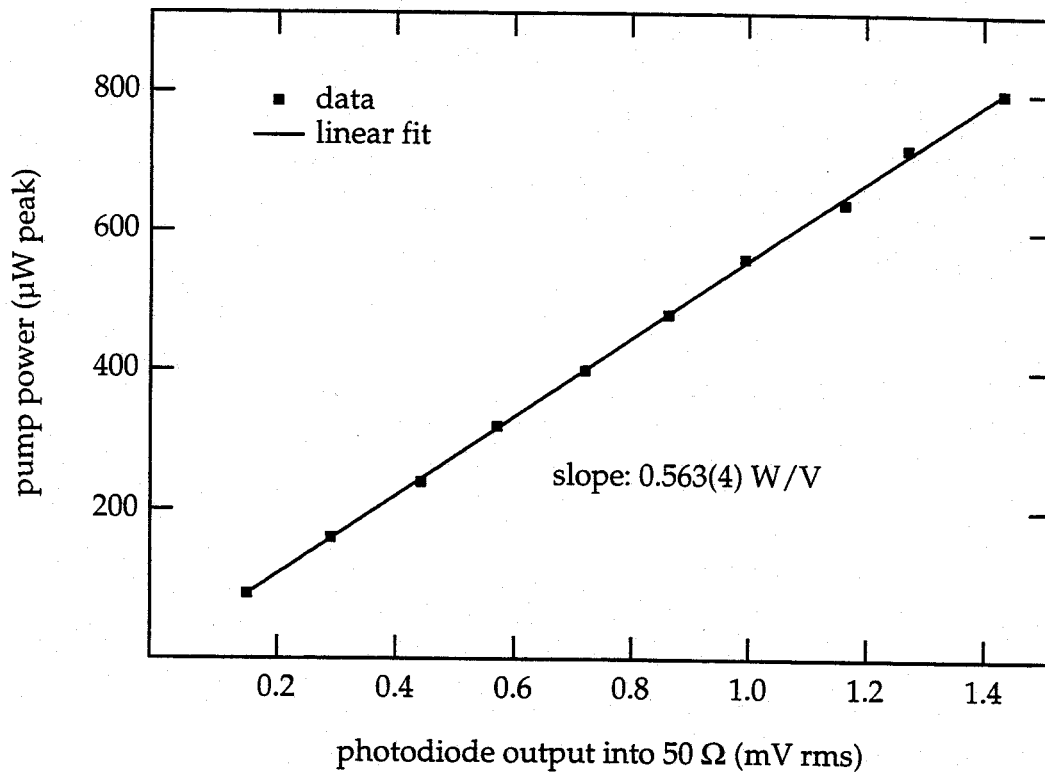
Figure 2.7. Calibration curve for clock-laser power-monitor photodiode.

the balance is disturbed by preferential absorption on either the high- or low-frequency side of the carrier. Phase-sensitive detection of the sideband imbalance leads to a dispersion-shaped line suitable for use as a frequency discriminator in a servo control loop.

The eom (New Focus model 4003) is constructed around a crystal of $LiNbO_3$ with ar-coated optically flat faces at normal incidence. A tank circuit, set to resonate at 10 MHz with a Q of approximately 50, enhances the drive voltage to the crystal. The eom drive signal originates from a Stanford DS340 synthesizer as a 10 MHz sine wave with a peak-to-peak amplitude of 3 V. The synthesizer output is coupled into the eom tank circuit via an impedance-matching transformer.

31
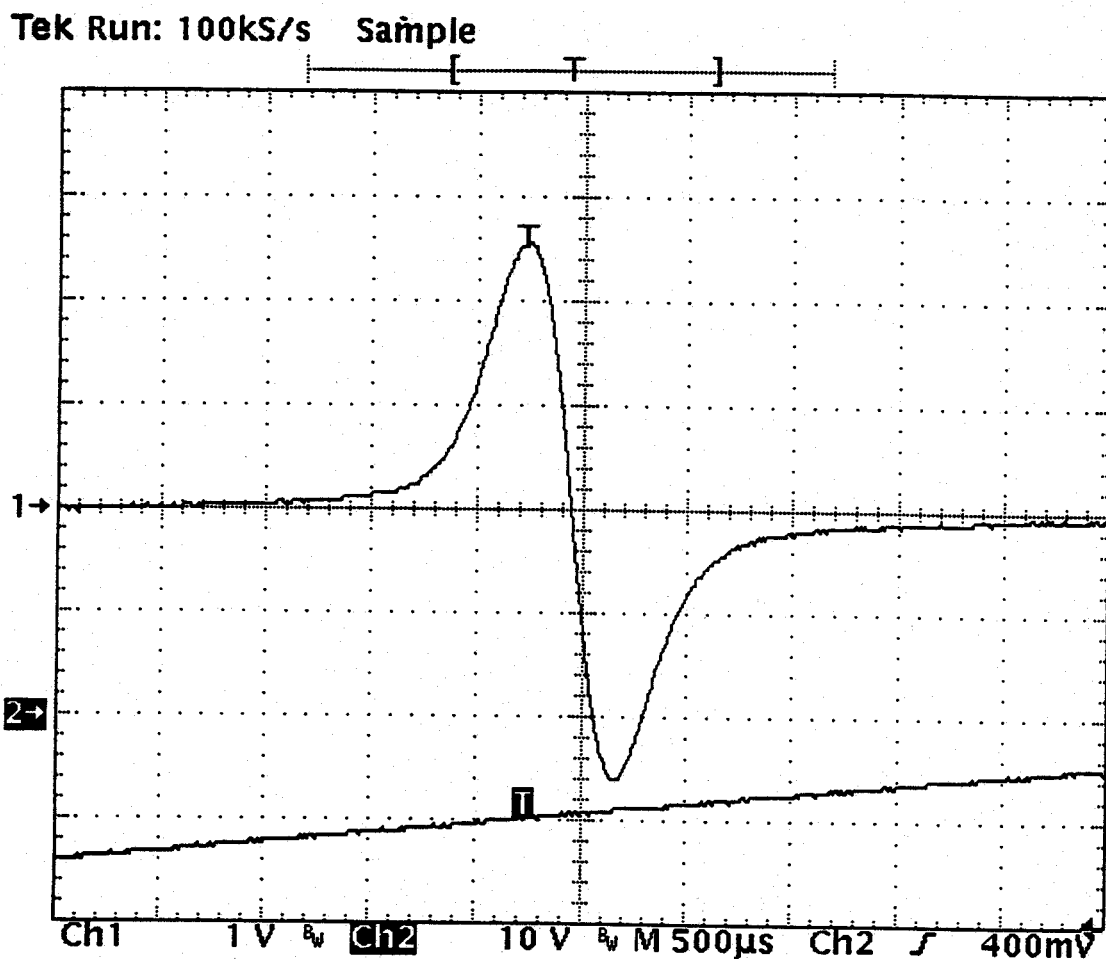
Figure 2.8. Dispersion line shape from the clock-laser frequency discriminator as observed on a Tektronix TDS 320 oscilloscope. The lower trace (channel 2) displays half the ramp voltage applied to the clock-laser pzt. The ^{3}He $2^3S_{1,F=1/2}$–$2^3P_{0,F=1/2}$ transition at 200 mTorr with a discharge supply voltage of 280 V is shown here. The sensitivity of the frequency-discriminator lock-in was set to give a reasonably large scope signal while its time constant was set to accommodate the sweep rate of the ramp; otherwise, conditions are identical to those used during data taking. Since the LNA laser tuning sensitivity is about 10 MHz/V, each major horizontal division corresponds to a 20 MHz change in laser frequency.

The probe absorption signal is detected with a 125 MHz photoreceiver identical to that used with the sweep laser. The fm signal at 10 MHz is isolated with a bandpass filter (Mini-Circuits model BBP-10.7) and then amplified by 20 dB with a Mini-Circuits ZFL-1000LN low-noise amplifier in order to provide additional gain for feedback purposes as discussed below. Phase-sensitive detection is accomplished by mixing the amplifier output with a 10 MHz reference in a Mini-Circuits ZAD-1-1 mixer. The reference is generated by a second Stanford DS340 synthesizer phase locked to the synthesizer which provides the eom drive. By varying the phase offset of the second synthesizer, the relative phase between the eom drive and the reference can be easily adjusted to optimize the detected line shape. The intermediate-frequency (if) port of the mixer is fed through a Mini-Circuits BLP-21.4 low-pass filter to remove any possible high-frequency pickup from, for example, the cell discharge circuitry. Just as for the sweep laser, a lock-in amplifier, with a 50 Ω termination and 177 kHz low-pass rc filter on its input, demodulates the 50 kHz chop impressed on the probe by the pump. The dispersion line shape for locking, observed by applying a ramp voltage to the clock-laser pzt and simultaneously monitoring the lock-in output, is shown in Figure 2.8.

The primary advantage of fm spectroscopy is that the high modulation rate, 10 MHz in the present case, permits detection at frequencies well above the laser technical noise. For the LNA lasers used here, the most prominent noise feature is a peak in the amplitude noise spectrum around 80 kHz, probably attributable to relaxation oscillation. Figure 2.9 depicts such a peak. The trace was obtained by directly monitoring the clock-laser 125-MHz-photoreceiver output with an HP70000 spectrum analyzer. Beyond this peak, the spectrum drops smoothly, reaching the shot-noise floor well before
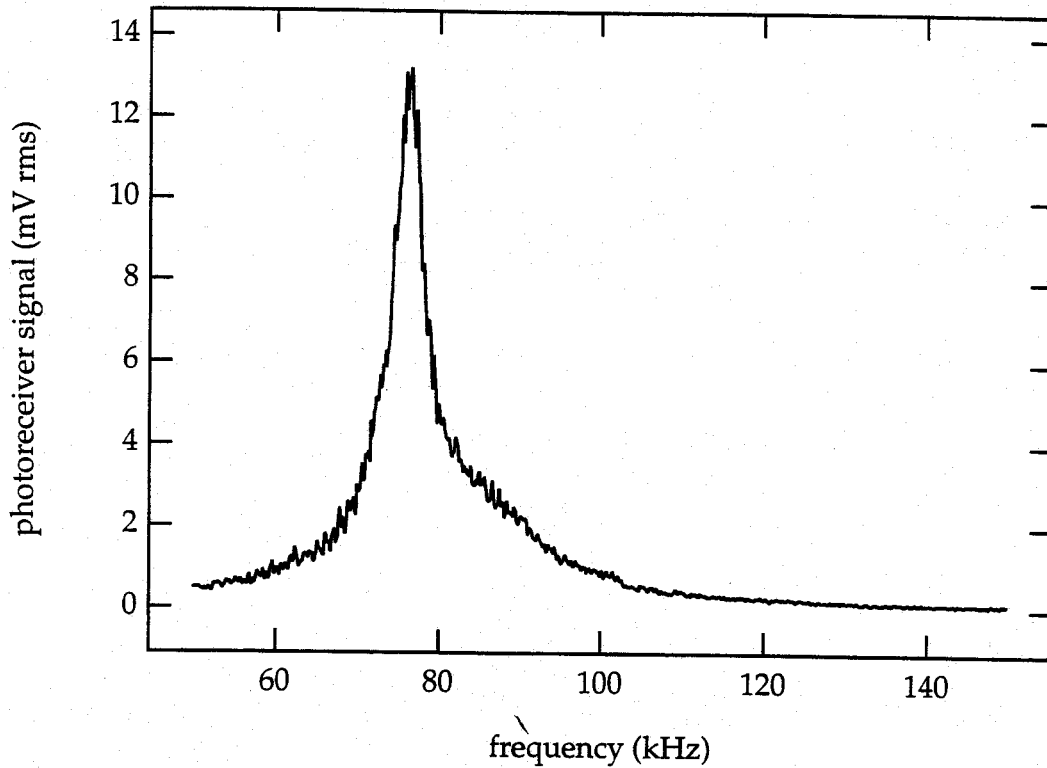
Figure 2.9. Spectrum of LNA laser amplitude noise.

1 MHz. The 10 MHz modulation frequency is chosen to be well into the shot-noise-limited region of the laser noise spectrum while remaining comparable to the line width of the helium transitions.

2.2.3 Frequency Stabilization of the Clock Laser

The frequency-discriminator signal, produced by fm spectroscopy, is fed back, via appropriate compensation electronics, to the high voltage amplifier controlling the pzt and hence the laser frequency. As can be seen in the lower part of Figure 2.4, this forms a servo control loop meant to lock the laser to

the line center. In designing this feedback system, the primary goal is achieving sufficient bandwidth and gain to correct for mechanical perturbations to the laser resonator. To measure fluctuations in the laser frequency, the feedback compensation shown in Figure 2.4 was replaced with a 0.1-s-time-constant electronic integrator in order to weakly hold the laser on the line center. Laser frequency jitter was thus converted into an error signal at the lock-in output which was then monitored with a Stanford SR760 spectrum analyzer. The spectrum analyzer directly displayed the Fourier components of the laser's frequency movements. All of the laser frequency fluctuations were found to be below 1 kHz and a spectrum-analyzer trace containing this region is shown in Figure 2.10. As can be seen, the spectrum
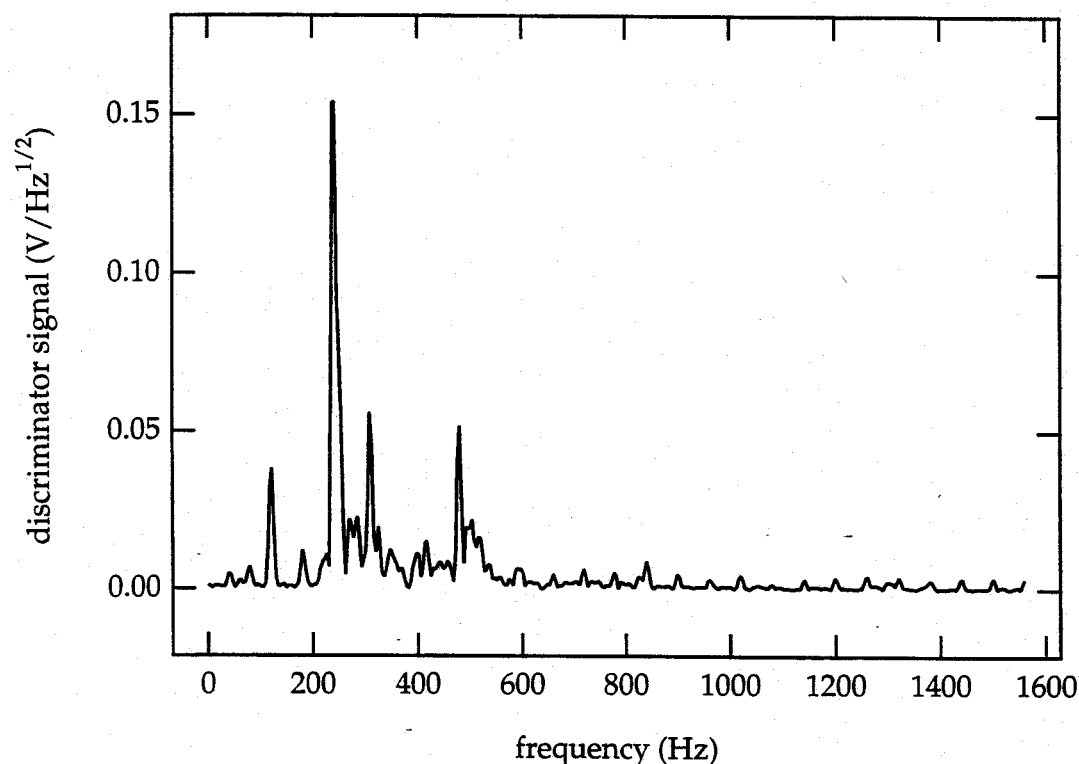
Figure 2.10. Spectrum of frequency jitter in the free-running clock laser.

consists primarily of a series of discrete peaks, probably corresponding to mechanical resonances of the cavity structure.

Performance of the clock-laser servo is optimized by maximizing the loop gain at the frequencies of the laser fluctuations while maintaining the conditions required for feedback stability. This is accomplished by inserting a suitably tailored feedback compensation network, as shown in Figure 2.4. In order to design this compensation element, the characteristics of the rest of the loop must first be determined. The transfer function of the loop without compensation was measured by using the integrator described above to center the laser on the line and then injecting a test sine wave through a summing junction at the input to the pzt high voltage amplifier. The test signal originated from the reference channel of a Stanford SR830 digital lock-in, which then measured the magnitude and phase shift of the loop response by sampling the output of the clock-laser frequency discriminator. The reference frequency of the SR830 was scanned under computer control while the loop response was recorded, resulting in the magnitude and phase plots of Figure 2.11.

The response shown in Figure 2.11 is dominated by contributions from three components of the feedback loop: the high voltage amplifier used to drive the pzt, the pzt itself, and the lock-in amplifier used to demodulate the 50 kHz aom chop. All other feedback elements have bandwidths far in excess of these and should present a negligible phase shift at the frequencies of interest. As a further diagnostic, a response plot was measured from each of the three elements.

The transfer function of the high voltage amplifier was measured using an SR830 lock-in to generate a test signal and measure the response of the instrument in a manner similar to that described above. Given the
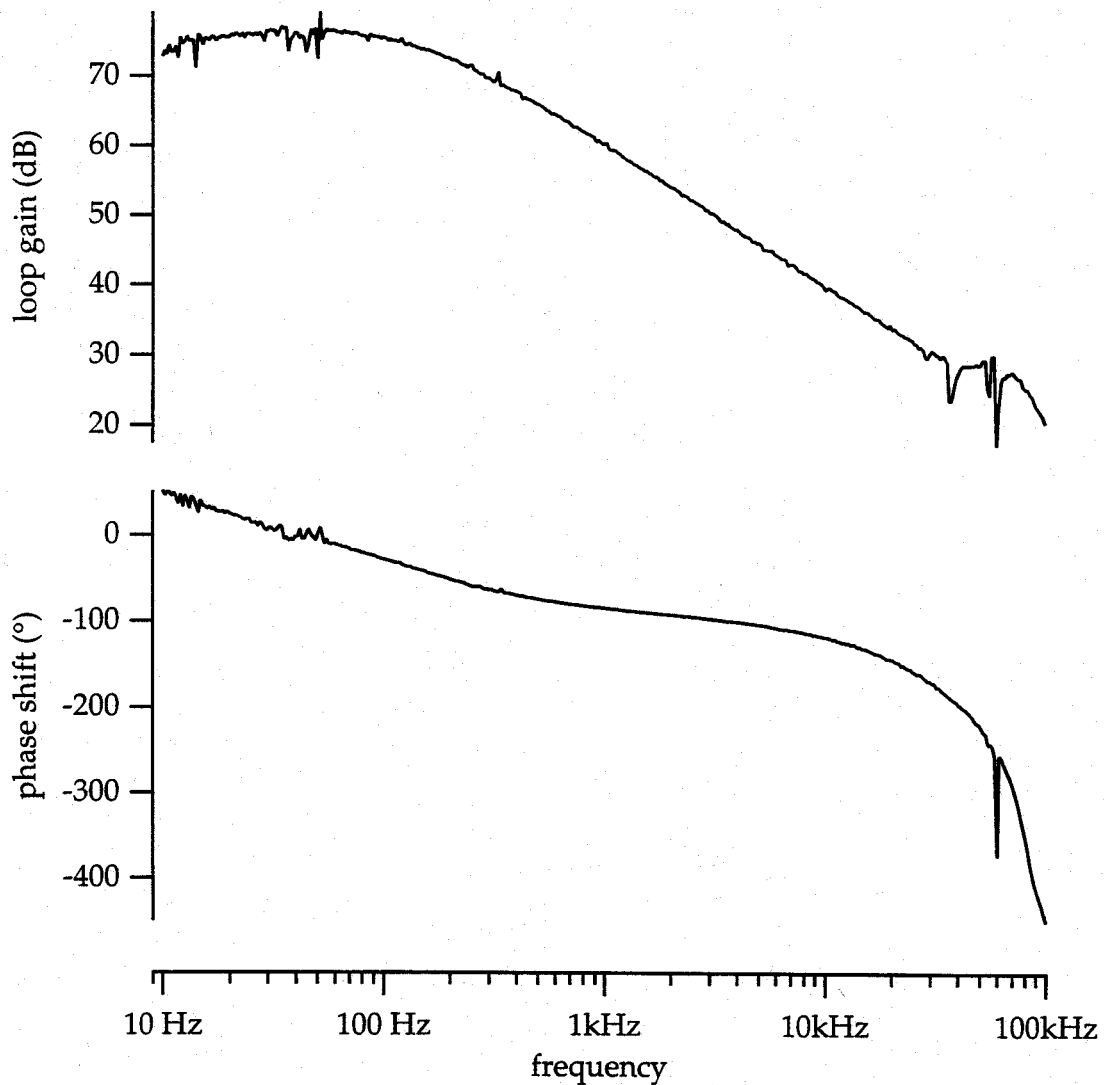
Figure 2.11. Response of the clock-laser servo loop in the absence of compensation. The low-frequency region is dominated by the lock-in pre-filter which has a 1 ms time constant. Note the pzt resonance peak near 60 kHz.

relatively large 1 MHz bandwidth of the high voltage amplifier, the fairly flat response curves which resulted, given in Figure 2.12, are not surprising. The
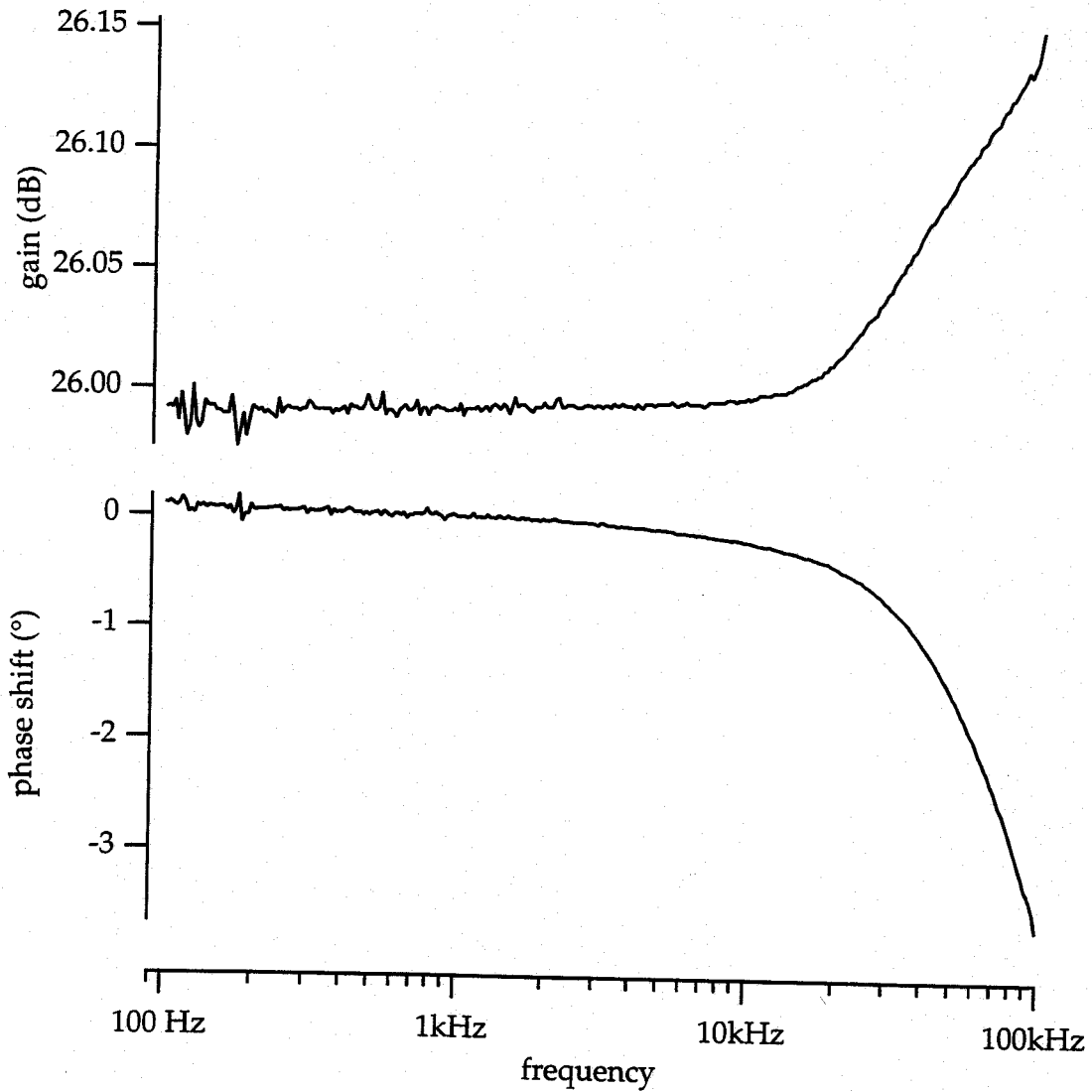
Figure 2.12. Transfer function of the Krohn-Hite KH7602 high voltage amplifier.

pzt's main contribution is its first mechanical resonance, which occurs at a frequency of approximately 60 kHz. This resonance was detected by driving the pzt directly with a sine wave, again from the lock-in reference channel, and sweeping the frequency. Upon reaching a resonance, the pzt current

draw would increase substantially resulting in a voltage drop across the 50 Ω output impedance of the lock-in reference port. Thus plotting the drive voltage as a function of its frequency gives the pzt resonance peak shown in Figure 2.13.
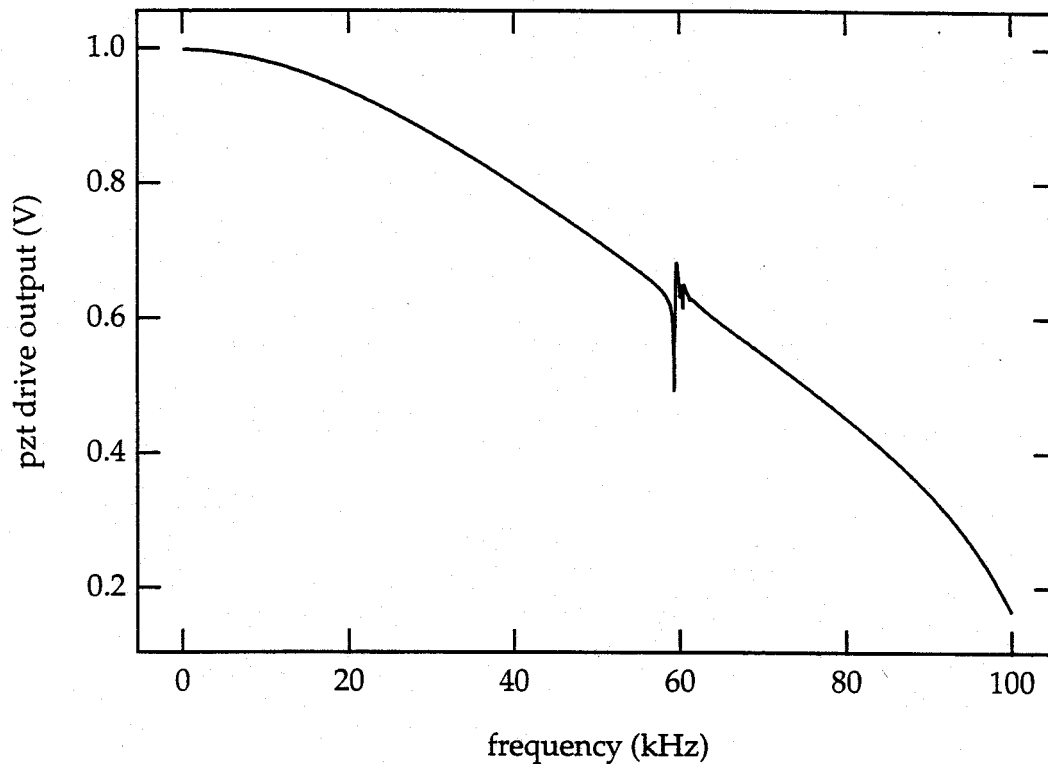
Figure 2.13. Pzt drive voltage versus frequency, showing a resonance near 60 kHz. The background slope results from the 53 kHz pole formed by the 60 nF pzt capacitance in conjunction with the 50 Ω drive output impedance.

Finally, the clock-laser lock-in was measured by impressing a test sine wave on a 75 kHz carrier through amplitude modulation. The lock-in removed the 75 kHz carrier and the test signal alone appeared on the output
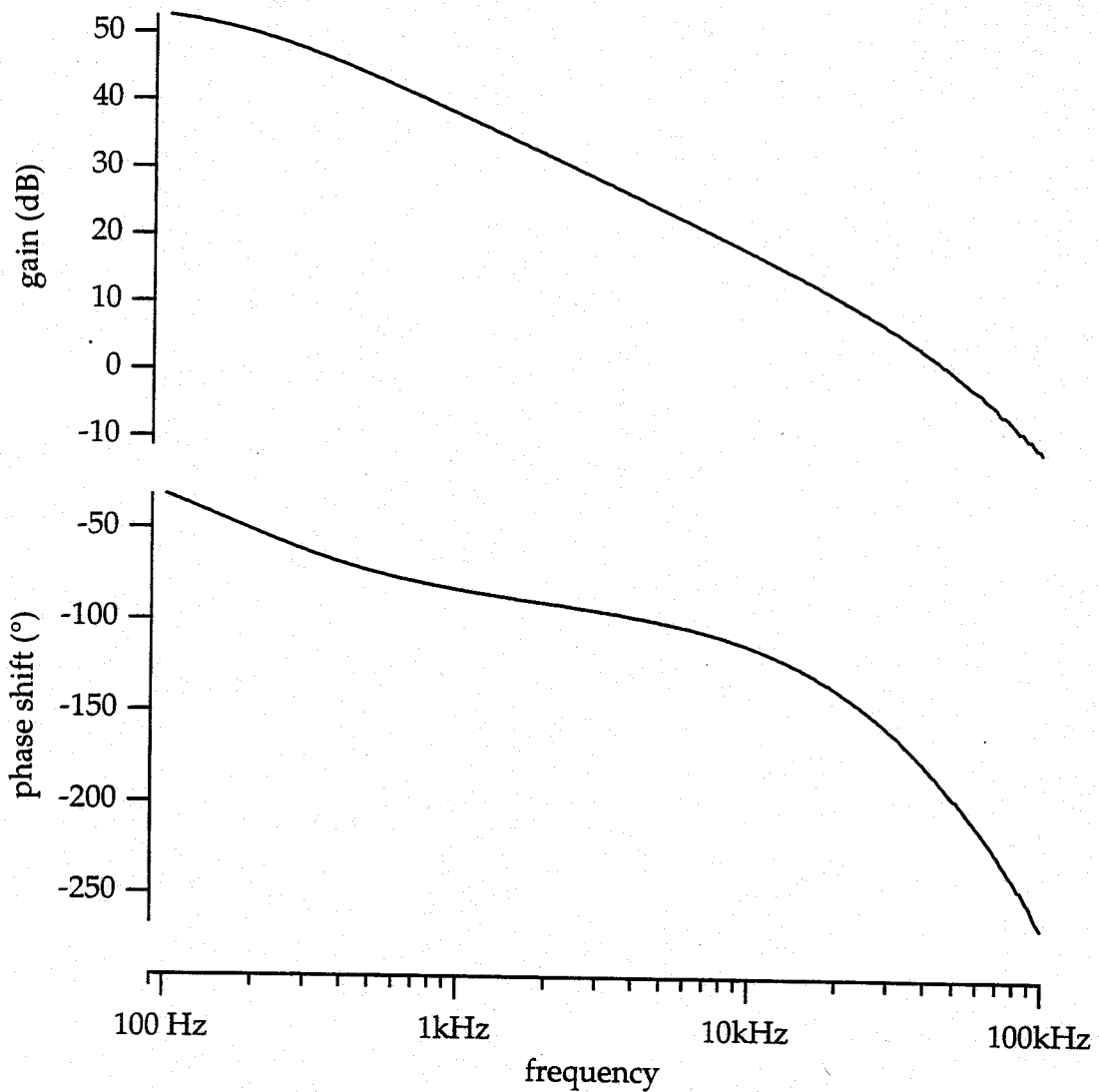
Figure 2.14. Response of the Stanford SR530 lock-in amplifier with a pre-filter time constant of 1 ms.

where its magnitude and phase were measured. Again, an SR830 lock-in was used to generate the test signal and obtain the response plots, which are displayed in Figure 2.14. It should be noted here that the clock-laser lock-in, which is the final stage of the frequency discriminator, is a Stanford SR530

analog lock-in. Although the time constant of this SR530 was always set to 1 ms for the frequency-servo purposes just described, its low-pass rc filter was modified to permit shorter time constants down to 10 μs. This was useful for measuring the spectrum of the laser frequency jitter where maximum lock-in bandwidth was desired. The digital SR830 lock-in was found to be unsuitable for inclusion in the feedback system because its internal digital signal processing was observed to result in a time delay of as much as 30–40 ms. Furthermore, aliasing effects would appear when the device was set at short time constants. Before continuing, it is perhaps useful to note that the measurements incorporated into Figures 2.11, 2.12, and 2.14 were taken with the clock-laser lock-in and high voltage amplifier gains reduced below the values in the figures. This was done in some cases to avoid saturation of the SR830 lock-in used to measure the response. An offset was then added to the magnitude plots to reflect the actual gain settings while the lock was engaged.
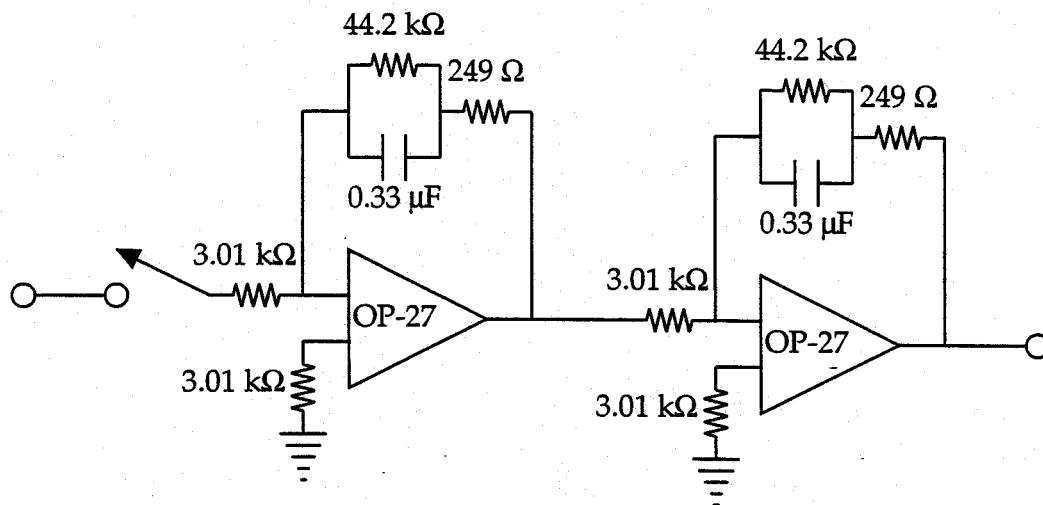
Figure 2.15. Compensation network for clock-laser feedback loop.

Even though the transfer function depicted in Figure 2.11 could, with attenuation, be used to form a stable feedback loop, the phase response would force an unacceptably low gain leading to poor suppression of laser frequency drift and noise. To permit higher loop gain, a compensation circuit, diagrammed in Figure 2.15, is inserted after the clock-laser lock-in. The
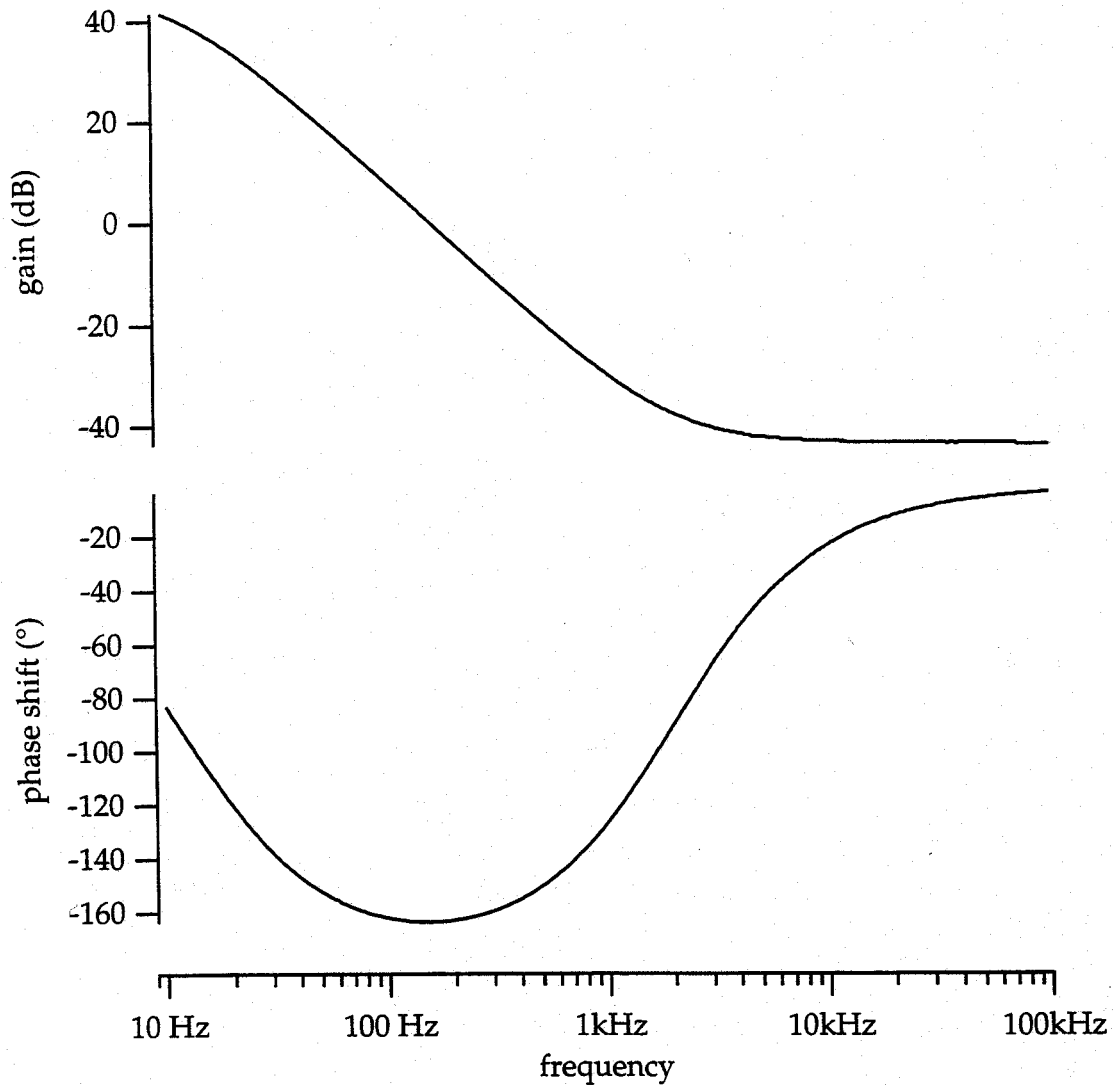
Figure 2.16. Transfer function of the clock-laser compensation network.

42

circuit consists of a double pole at 11 Hz and a corresponding pair of zeroes at 1937 Hz. The measured transfer function, taken in the usual way with a lock-in, is shown in Figure 2.16.

Concatenating this response to that given in Figure 2.11 results in a
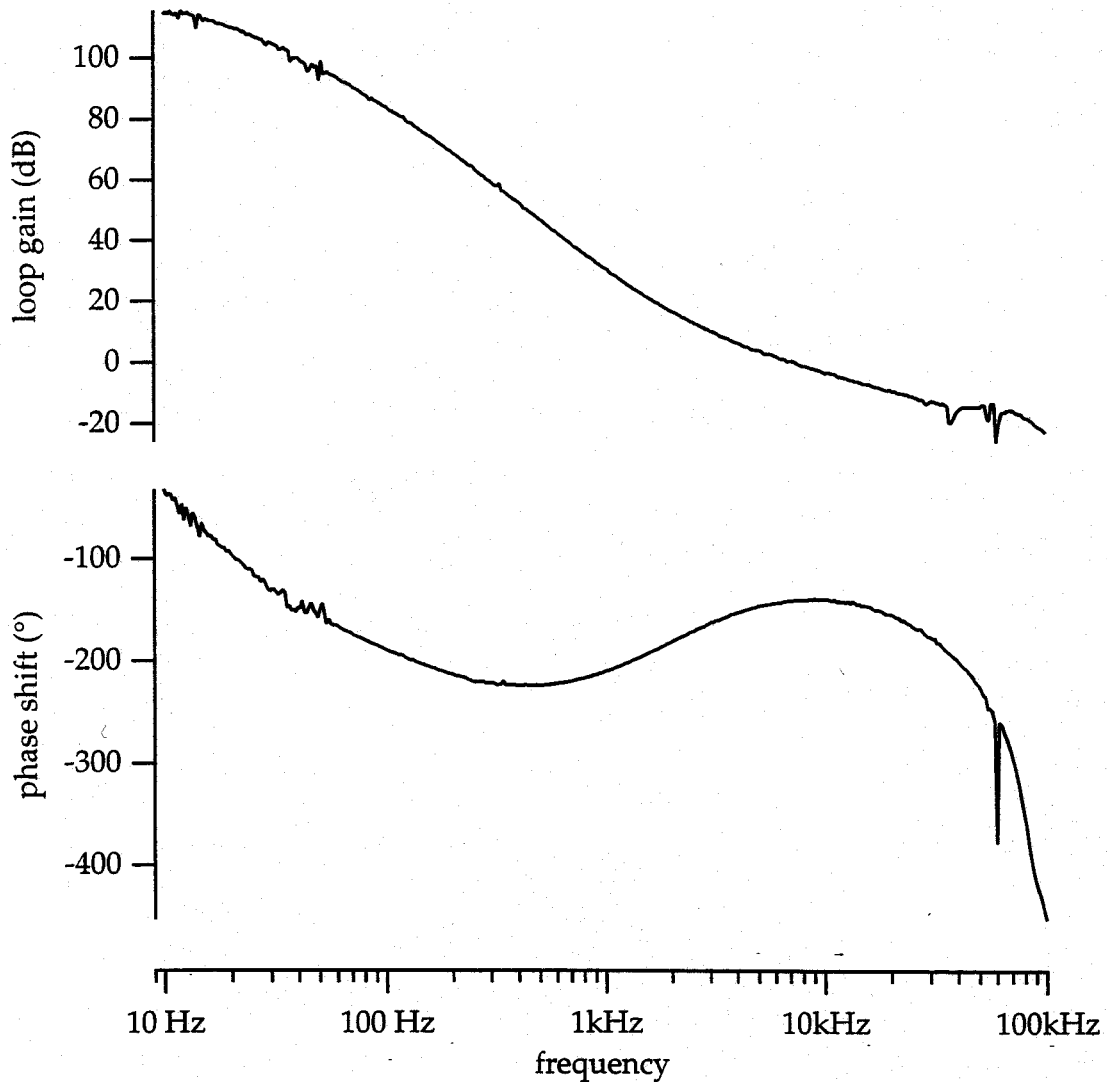
Figure 2.17. Response of the complete clock-laser servo loop including compensation.

plot of the complete loop gain and phase shift, displayed in Figure 2.17. The Bode plot, in the upper half of Figure 2.17, exhibits a dc gain of approximately 115 dB and then begins a 12 dB per octave descent at the double pole, steepening to 18 dB per octave at the 159 Hz pole contributed by the SR530 lock-in low-pass filter. The two zeroes reduce the slope to 6 dB per octave and the curve crosses unity gain at about 7.5 kHz with a phase margin of 40°. With the loop closed, the error signal at the SR530 lock-in output showed no substantial deviation from zero when monitored with an oscilloscope.

2.2.4 Frequency-Offset Lock Between the Clock and Sweep Lasers

The frequency of the sweep laser is controlled by mixing its beam with that of the clock laser on a high speed photodiode and locking the heterodyne signal to a stable rf source with a phase-locked loop. The sweep laser is then scanned by varying the frequency of the rf source. As depicted in Figure 2.2, portions of the clock and sweep laser outputs are combined on a beamsplitter and then sent through a telescope with a 16:1 demagnification. The telescope and a grin rod attached to the end of a single-mode fiber provide coupling into the fiber with an efficiency of about 70%. The 30 m length of fiber leads via an ST connector into a high speed photodiode (New Focus model 1011) with a bandwidth of 40 GHz. Generally about 0.5 mW of light from each laser reaches the photodiode. The heterodyne signal from this detector is ultimately routed into an EIP578B source-locking microwave counter. A diagram of the frequency-offset system is shown in Figure 2.18.
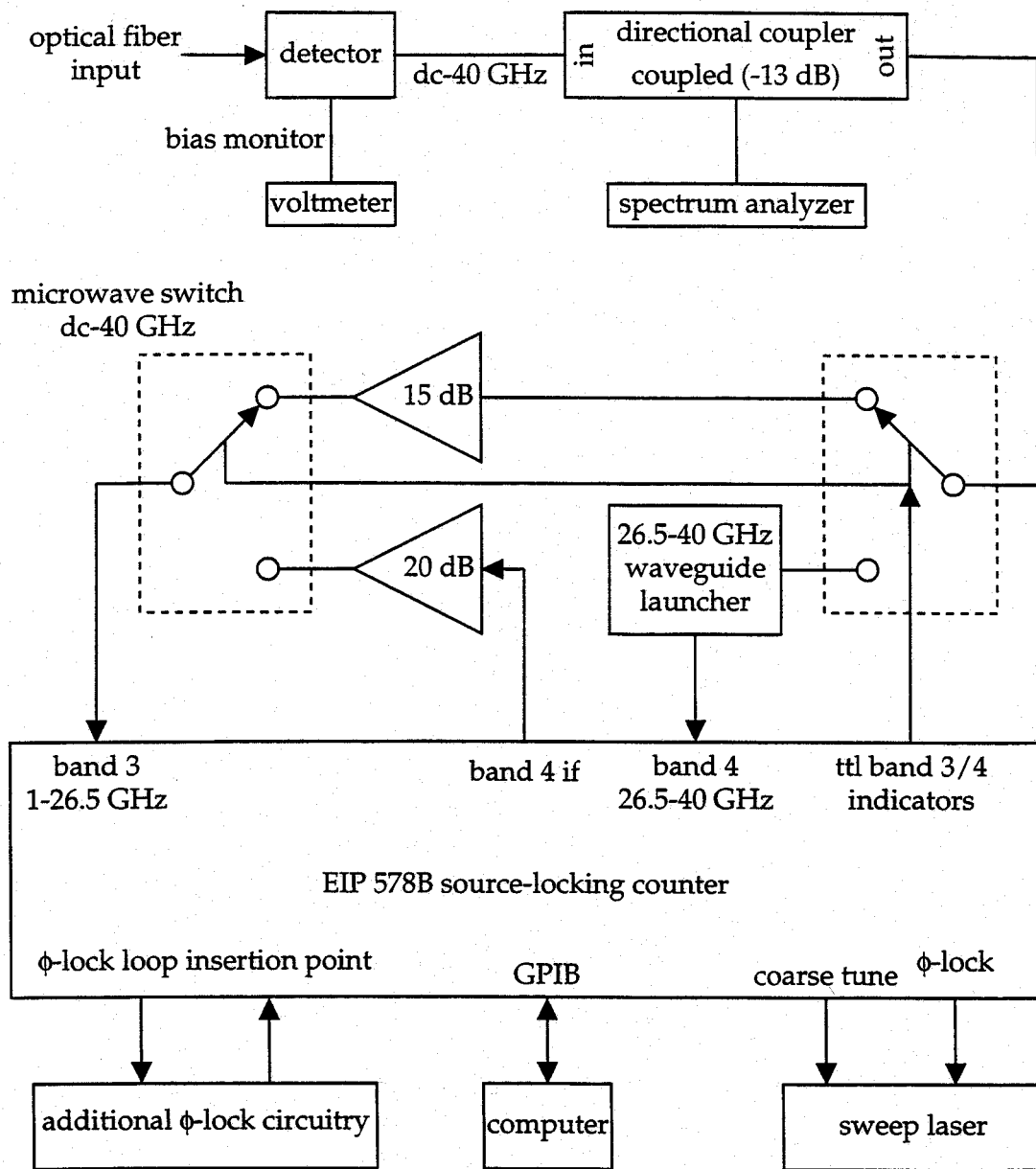
Figure 2.18. Simplified diagram of the system for frequency-offset locking.

The center piece of the offset locking apparatus is the EIP578B counter. In addition to a frequency down-conversion chain, the instrument houses a phase-locked loop referenced to a programmable internal synthesizer. Thus

the input frequency can be electronically compared to a designated frequency in order to generate an error signal for locking purposes. The counter has four inputs corresponding to different frequency bands: band 1 for signals from 10 Hz to 100 MHz, band 2 for 10 MHz to 1 GHz, band 3 for 1 to 26.5 GHz, and band 4 for 26.5 to 110 GHz. Band 4 is further subdivided into band 4-1 for 26.5–40 GHz, band 4-2 for 40–60 GHz, band 4-3 for 60–90 GHz, and band 4-4 for 90–110 GHz. These sub-bands correspond to different choices of an external mixer diode. For the frequencies encountered in the present experiment, only bands 3 and 4-1 are used. When band 4-1 is in use, an intermediate frequency (if) is generated on the front panel at a port which must then be patched into the band 3 input. The counter is manually set at one of the two bands depending on the heterodyne frequency.

Custom modifications to the counter were made by the manufacturer to provide ttl-level signals from the rear panel indicating whether the device is operating in band 3 or 4. This band 3/4 indicator controls two spdt microwave switches (Dynatech model DK1-916E70L) which determine the path for the heterodyne signal. Upon originating at the photodiode, the laser beat note is sent through a high frequency K connector to a 1–40 GHz broadband directional coupler with a -13 dB coupled port, which is used to monitor the photodiode output with a spectrum analyzer. After the directional coupler, the signal is routed by the switches, which are electromechanical devices rated for low insertion loss from dc to 40 GHz. If the counter is set for band 3, the signal is boosted by at least 16 dB with an HP8349B microwave amplifier and then fed to the band 3 input. If the counter is set for band 4, the beat note is sent to a Ka-band waveguide launcher mated to the band 4 input port. This connection is the only one in the system requiring a waveguide component; all others employ high

frequency coax-type connectors. The band 4 signal is mixed down in the instrument to produce the band 4 if output with a frequency in the range 1–1.35 GHz. This if signal goes through a 20 dB amplifier (Anzac model AMC-184) before being routed to the band 3 input by one of the microwave switches. The HP and Anzac amplifiers serve to increase the band 3 input power significantly above the specified detection threshold of -30 dBm. In addition, the band 4-1 external mixer diode was preselected for enhanced sensitivity, though it was later found that the 20 dB if amplifier was nevertheless required for robust operation. Basically, both amplifiers were included because the high speed photodiode can provide only about -33 dBm of microwave power with 1 mW of incident light.

The sweep laser is controlled by two outputs of the counter: an error signal generated by the phase-lock loop and a coarse-tune voltage used by the counter to keep the external source within the capture range of the phase-lock loop. Both outputs are summed at the sweep-laser high voltage amplifier. To perform a frequency scan, the thick etalon of the sweep laser is tuned to insure that no mode hop occurs within the scan interval. The counter is then instructed by computer to lock the sweep laser to a sequence of frequencies traversing the region of interest. At each point, the actual difference frequency between the lasers is independently measured by the counter while the lock is engaged.

With the system described above, it was found that the locked offset frequency would still exhibit fluctuations of order 100 kHz. To remedy this, the feedback compensation within the counter was modified to introduce additional gain. It is known that the unmodified loop gain of the counter crosses unity near 10 kHz. A lag network, shown in Figure 2.19, containing a pole at 53 Hz and a zero at 3189 Hz was inserted into the servo loop. As seen
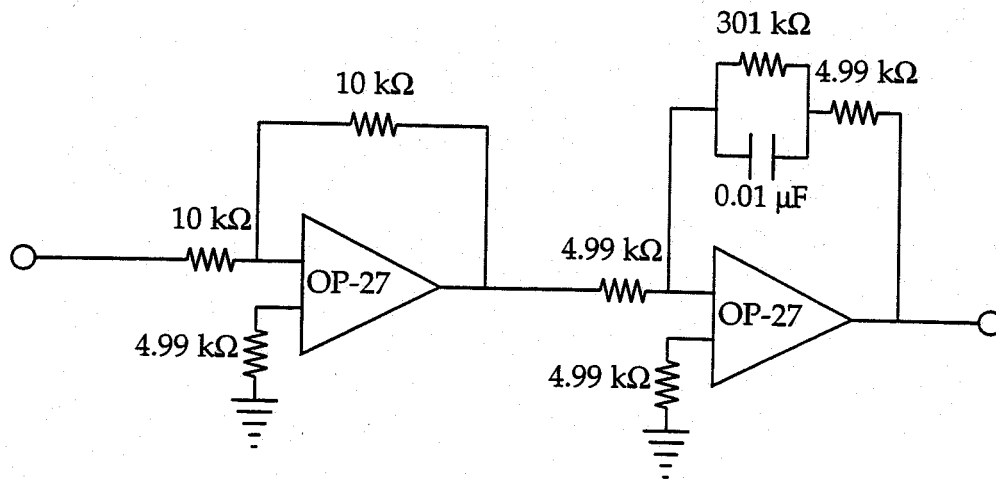
Figure 2.19. Additional feedback circuitry for the EIP578B source-locking counter.

in the response plot given in Figure 2.20, this circuit provides an additional gain of 36 dB at dc but leaves the original loop transfer function relatively unchanged around its unity-gain crossing thereby preserving the stability.

The EIP578B counter is a highly automated microprocessor-controlled device which, among many other things, attempts to determine the tuning sensitivity of the external source by measuring the frequency change in response to a voltage step in the phase-lock error signal. This information is then used to set an attenuator in the feedback loop to give the proper overall gain before locking to the target frequency. Unfortunately, the rather large and fast frequency fluctuations in the unlocked sweep laser often caused the counter to arrive at an inaccurate value for the tuning sensitivity. This would then result in an incorrect gain setting and poor servo performance. It was thus necessary to instruct the counter to overwrite its automatically determined attenuator setting with a new, correct value obtained beforehand
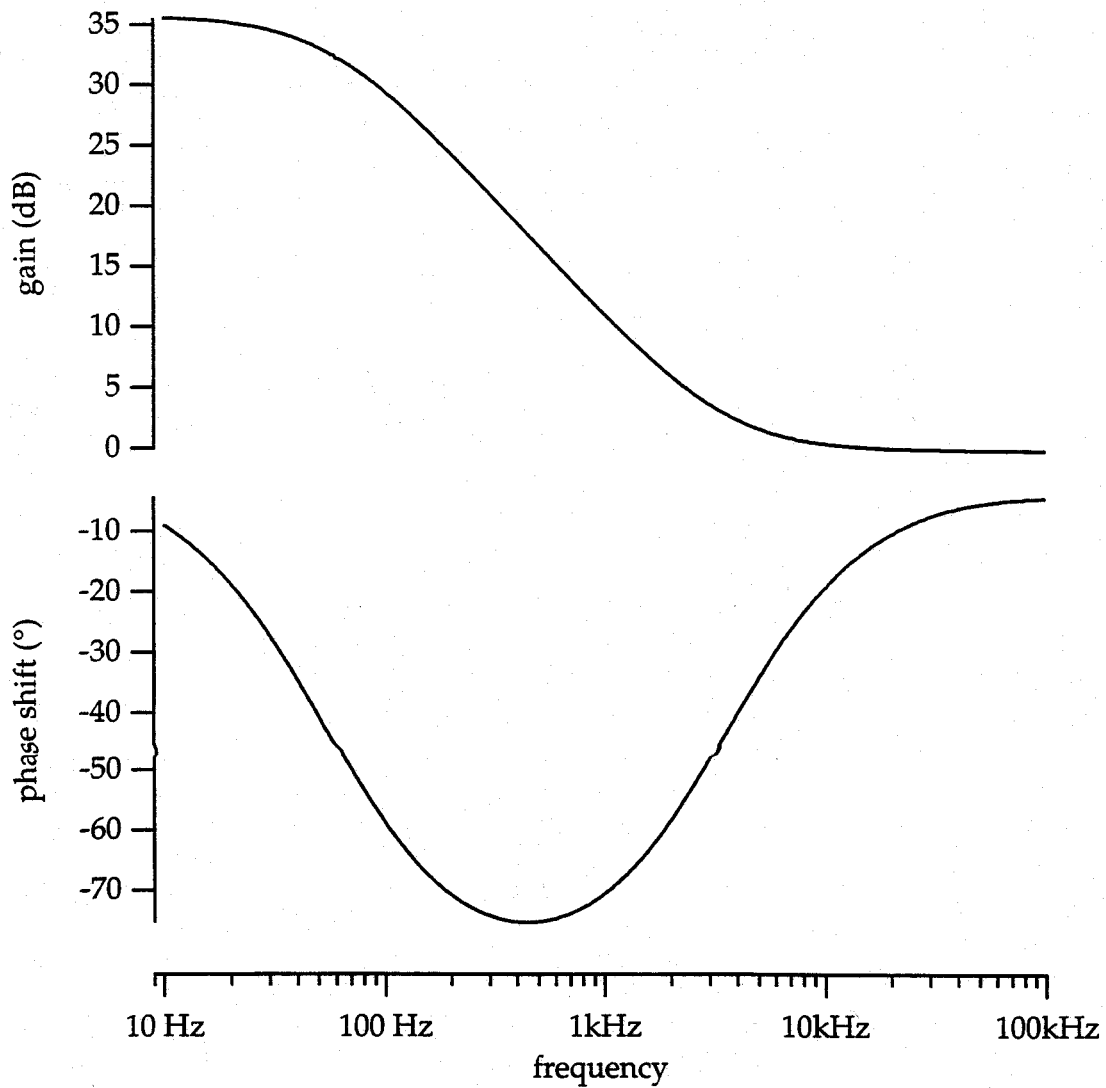
Figure 2.20. Response of the EIP578B lag network.

by experimenting with the attenuator setting. This overwrite procedure was issued by computer at each point in a frequency scan.

2.2.5 Performance of the Frequency Servos

The frequency stability of the clock laser was gauged by heterodyning its output against that of an identical but independent system formed by inserting an eom and locking electronics into the sweep-laser apparatus. With the clock laser locked to the ^{3}He $2^3S_{1,F=1/2}$–$2^3P_{0,F=1/2}$ line and the sweep laser to one of the ^{4}He 2^3S_1–$2^3P_{0,1,2}$ lines, the beat note generated at the New Focus 1011 photodiode was monitored with the EIP578B microwave counter. The frequency displayed by the counter was plotted as a function of time; such
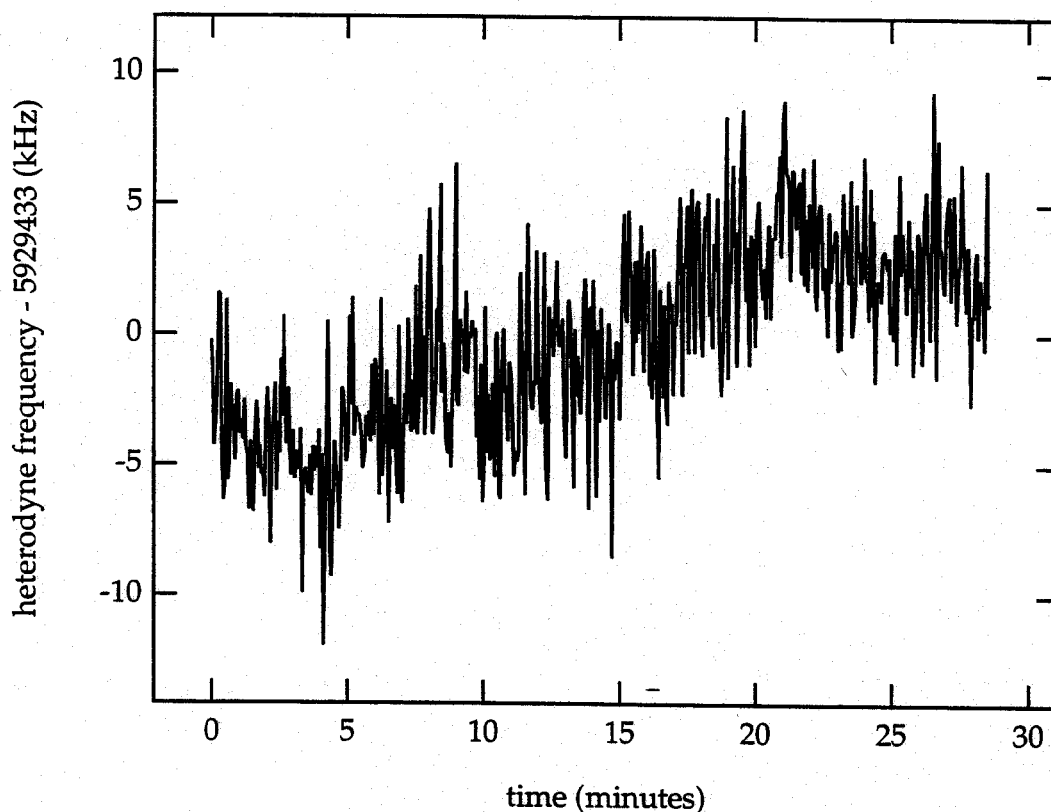
Figure 2.21. Difference frequency between two locked lasers as a function of time.

a graph is shown in Figure 2.21. As seen in Figure 2.21, the heterodyne frequency was found to drift by roughly 10 kHz over a period of twenty to thirty minutes, though more abrupt transitions would occur sporadically. Within a time frame of several hours, the frequency generally wandered back and forth, remaining within 10–20 kHz of a central value.

At this time, the physical mechanism underlying the frequency drift has yet to be conclusively determined. One possible culprit is the presence of residual amplitude modulation (ram) from the eom. In this scenario, the eom, in addition to producing phase-modulation (pm) sidebands, also generates low-level amplitude modulation (am) at the same frequency. The addition of the am sidebands disturbs the balance of the pm sidebands and causes an offset in the lock point. Changes in the level of ram with time would give different offsets and thus a drift in the heterodyne frequency. Previous investigations [37] have indicated that a primary source of ram is optical interference arising from scattering and multiple reflections within the eom crystal. Given the short wavelengths involved, thermally driven changes in optical path length could easily result in time dependence of the ram.

This model is consistent with a number of observations. With the clock and sweep lasers locked to their respective lines, the heterodyne frequency differs by 100–200 kHz from the value one would expect based on the measured ^{3}He–^{4}He isotope shift. This appears to be clear indication of an offset in the lock. Furthermore, the relatively slow rate of the drift would seem to implicate some sort of thermal effect. Direct observation of the light intensity at the eom output with a photodiode attached to a spectrum analyzer clearly revealed amplitude modulation with a level that changed on the same time scale as the frequency drift. Finally, it is known that pure
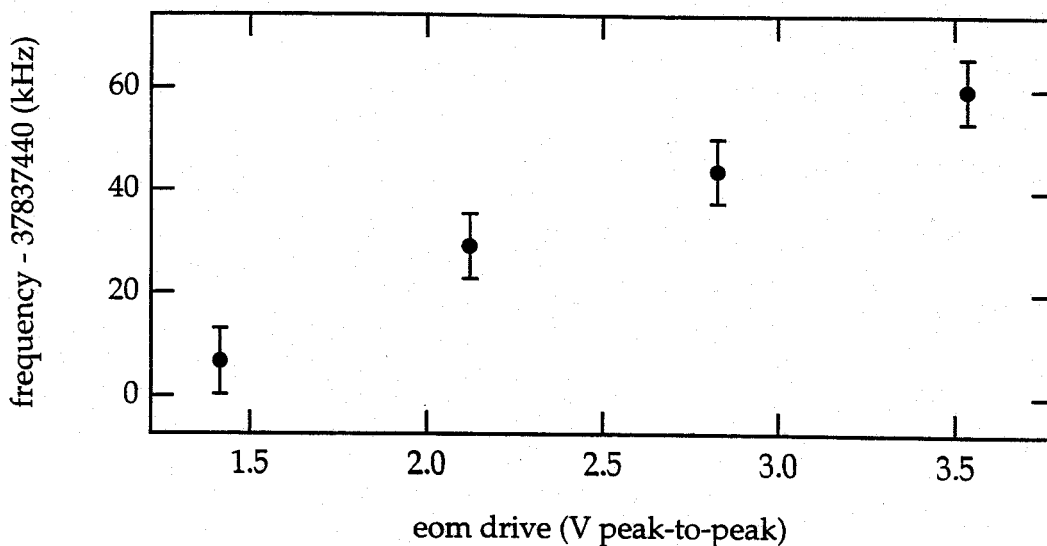
Figure 2.22. Difference frequency between the two locked lasers as a function of the drive voltage to each eom. The error bars reflect the size of the frequency drift observed during the period over which the data was taken.
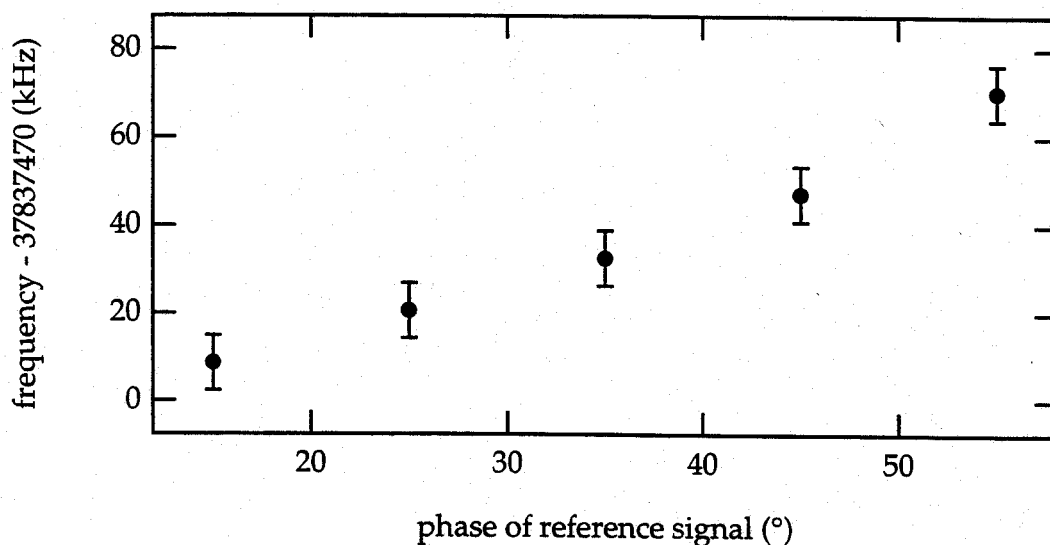
Figure 2.23. Difference frequency between the two locked lasers as a function of the demodulation phase for each eom. The error bars reflect the size of the frequency drift observed during the period over which the data was taken.

phase modulation gives a dispersion line shape with odd symmetry regardless of the eom drive voltage or the phase of the demodulating reference signal. The lock point should thus be independent of both parameters. However, as depicted in Figures 2.22 and 2.23, the difference frequency was found to vary with the drive strength as well as the demodulation phase, perhaps indicating the presence of a component other than phase modulation. Drift in the clock-laser frequency is presently a major limitation of the experiment. Possible means to improve the stability are discussed in Chapter 4.

The offset servo controlling the sweep-laser frequency with respect to that of the clock laser exhibits no significant long-term drift. However, rapid fluctuations in the beat frequency, as displayed by the counter, have been observed and can be as small as ± 2 Hz or as large as ± 2 kHz. When this frequency noise is small, a spectrum-analyzer trace of the heterodyne note, given in Figure 2.24, reveals that the feedback loop has captured a substantial portion of the signal within a narrow 20–30 kHz wide peak. On the other hand, a trace, displayed in Figure 2.25, taken in the presence of the largest frequency fluctuations shows only a broader 250 kHz wide peak. It is not clear what is responsible for this wide variation in servo performance. Although the effect seems unimportant at the present level of accuracy, it will obviously require investigation as the experiment is refined.

Figure 2.24. Spectrum of the heterodyne signal with the frequency-offset servo engaged. This trace was taken while small fluctuations (± 2 Hz) were observed in the counter reading. The graph was generated directly from the plotter output of an HP70000 spectrum analyzer. Given the 1 MHz span, each horizontal division corresponds to 100 kHz.
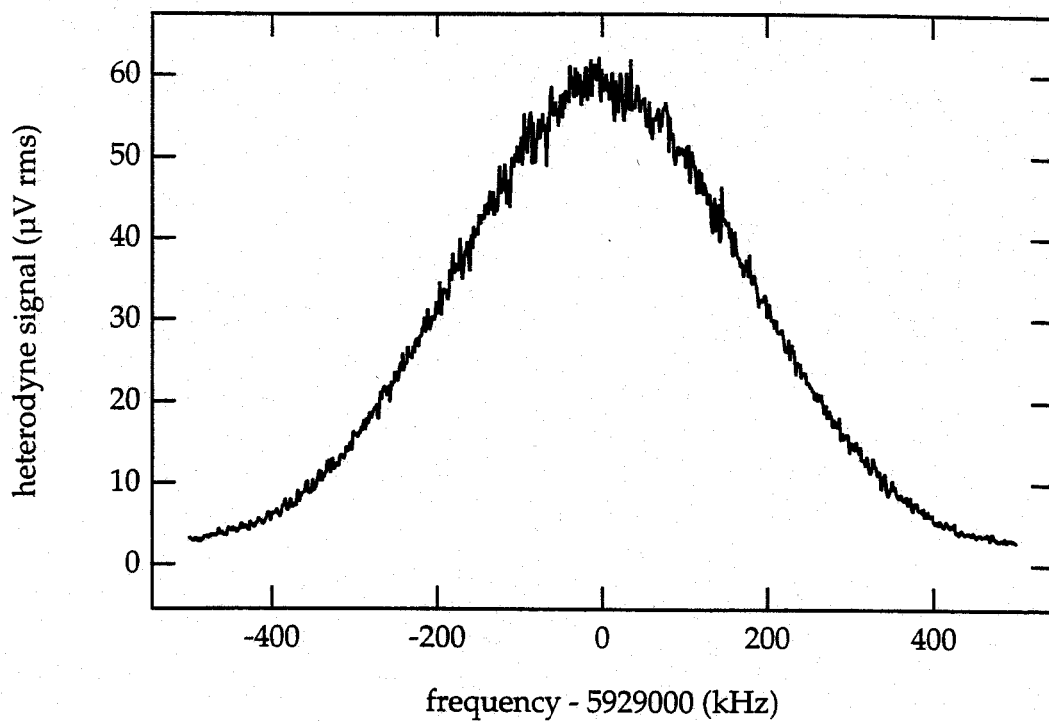
Figure 2.25. Spectrum of the heterodyne signal with the frequency-offset servo engaged. This trace was taken while large fluctuations (± 2 kHz) were observed in the counter reading.

Chapter 3

Data Acquisition and Analysis

The fine-structure splittings in ^{4}He were observed as outlined in Chapter 2: the sweep laser was tuned across each of the 2^3S_1–2^3P lines by varying the difference between its frequency and that of the clock laser. This method gives results which are insensitive to any constant offset in the clock-laser lock point and are thereby immune to the time-independent component of residual amplitude modulation (ram) in the eom. Due to its interferometric origin, ram is a particularly insidious phenomenon that can vary not only with time but also with optical wavelength and even across the wavefront of the beam. The present technique also permits careful examination of the line shape for evidence of other systematic errors. Of course drift in the frequency of the clock laser, as discussed previously, remains a serious limitation. Quantifying such imperfections in the experiment to arrive at an accurate estimate of the measurement uncertainty is a crucial part of all precision measurements.

To search for systematic shifts, line centers were measured under different values for three parameters of the sweep-laser spectrometer:

1) ^{4}He cell pressure,

2) pump and probe beam intensity, and

3) strength of the rf discharge as determined by its supply voltage.

The end results were arrived at after considering all observed effects. The remainder of this chapter details the steps taken to obtain the data and extract the required values for the fine-structure intervals.

3.1 Procedure for Data Taking

The data consists entirely of traces by the sweep laser over each of the 1083 nm ^{4}He lines. In all instances, the clock laser was locked to the ^{3}He $2^3S_{1,F=1/2}$–$2^3P_{0,F=1/2}$ transition within a 200 mTorr discharge cell. This transition was chosen to generate a heterodyne frequency which would fall within either band 3 or band 4-1, depending on the ^{4}He line, of the EIP578B counter. The higher pressure 200 mTorr cell and a nearly maximum discharge supply voltage of about 280 V were used in an attempt to maximize the absorption signal. The rate of mode hops and frequency drift in the lasers often appeared to be substantially lower during late-night hours, say from 11 pm to 6 am, perhaps indicating better temperature stability in the laboratory during this period. Of course general inactivity in the building at these hours also greatly reduced the degree of mechanical disturbances. All data was thus collected during such late-night intervals. For each data-taking session, either the laser-power or discharge-voltage dependence of all three ^{4}He lines was

studied for a given cell pressure. One night of run time was usually sufficient to obtain about twenty scans distributed among the three transitions.

All parts of the experiment were turned on at least one to two hours prior to data collection to allow a "warm up" period. In particular, this insured that the oven-stabilized crystal time base in the EIP578B counter and the rf discharge apparatus would reach a stable equilibrium. Because of the long life of the pump laser diode arrays, both LNA lasers were run continuously over the several months required for troubleshooting and data acquisition. The clock and sweep lasers were tuned to their respective helium transitions by tilting the etalons and varying the dc offset of the KH7602 high voltage amplifier for each laser. Some effort was made to closely center each etalon at the transition frequency by maximizing the laser output power from the appropriate cavity mode and arranging for the helium line to be midway between mode hops induced by scanning the pzt over more than one fsr. Adjustment of the tilt of the output coupler and translation of the diode pump beam was often required to give a single transverse mode with adequate output power. Single-mode operation was monitored on a Burleigh optical spectrum analyzer with an fsr of 8 GHz and a resolution bandwidth of order 80 MHz. To detect nearly degenerate transverse modes unresolved by the optical spectrum analyzer, a fast ramp voltage, as seen in Figure 2.8, was applied to the pzt and the helium line shape, typically with a width of about 10 MHz, was observed on an oscilloscope for evidence of additional modes. Upon completion of its tuning procedure, the frequency servo for the clock laser was engaged. It was found that the frequency lock could be sustained for the duration of a night's data run by just periodically nulling the error signal with the dc offset to the pzt and without further adjustment to the clock-laser optics.

Scans by the sweep laser are controlled by a computer program which can be instructed to record the data associated with each trace to a file. Before the start of each scan, the program logged a set of experiment parameters including:

1) the date and time at the start of the scan,

2) the transition excited by each laser,

3) the pressure of each helium cell,

4) the discharge supply voltage for each cell,

5) the voltage from the power-monitoring photodiode for each LNA laser,

6) the values of the neutral-density filters used to adjust the optical power incident on the sweep-laser helium cell,

7) the frequency and amplitude of the eom drive,

8) amplifier gains in the frequency-control electronics,

9) the sensitivity and time constant of the sweep-laser lock-in.

The computer then took the line shape by instructing the offset servo to lock to a sequence of equally spaced frequencies traversing the desired span. A sweep consisting of 100 points within a 50 MHz interval centered at the transition was employed for all data presented in this chapter. Before closing the lock at each frequency, the computer would, as discussed in Section 2.2.4, override the EIP578B counter's internal logic and set the loop attenuator to a value which gave better performance. In order to allow a conservative settling time, a delay equal to ten times the sweep-laser lock-in time constant was inserted after acquisition of the phase lock. For all present data, the lock-in (Stanford SR830) had a time constant of 100 ms and a filter slope of 24 dB per octave. Following the delay, the heterodyne frequency from the counter, the magnitude of the saturated-absorption signal from the sweep-laser lock-

in, and the sweep-laser power as seen by its monitor photodiode were read to produce one point in the trace. Should the offset lock be broken, *e.g.*, by a laser mode hop or vibrations, the counter would attempt to reacquire lock using its internal logic thereby incorrectly setting the loop attenuator. To guard against this condition, the computer checked *the loop attenuator setting after taking the data for each point*. If the value were unchanged then the computer would proceed to the next step; otherwise it would discard and remeasure the point. For each trace, the computer program was restarted with the sweep-laser transition and experiment parameters set appropriately.

3.2 Data Reduction and Error Analysis

Data were collected with all three cells containing ^{4}He at pressures of 50 mTorr, 100 mTorr, and 200 mTorr, respectively. For each cell, scans of the three transitions were taken with a range of optical excitation intensities. Although the saturated-absorption pump and probe beams have separate neutral-density-filter attenuators, all data were obtained with equal optical density values in each arm thus maintaining the pump/probe power ratio near 1.7. For this measurement, the pump power was varied within a range of about 5–25 μW with a proportional change in probe power. For the 50 and 200 mTorr cells, traces were also taken at different discharge supply voltages spanning a range of 75 or 80 V. To exclude errors from possibly large day-to-day changes in the clock-laser lock point, comparisons involving frequency were made only between lines taken in a single night's run. Thus values for the fine-structure splittings were always derived as differences between line centers from the same run. Furthermore, in an attempt to gauge the clock-

laser frequency drift during the course of a data-taking session, line scans were repeated at various intervals as a check of reproducibility. Since about twenty sweeps could be accommodated in each run, only a rather sparse set of data could be gathered per night for each transition.

Typical examples of lines obtained under various conditions of cell pressure, laser power, and discharge strength are shown in Figures 3.1–3.3. The bottom portion of each figure shows the line trace together with a fit to a function of the form

$$f(v) = \frac{a}{\left\{ \left[\frac{2(v - v_0)}{\Delta v} \right]^2 + 1 \right\}^x} + b(v),$$ (3.1)

where a is the amplitude, v_0 the line center, and $b(v)$ a polynomial representing the baseline with terms up to third order. The full width at half maximum of the peak is given by

$$\text{fwhm} = \Delta v \sqrt{2^{\frac{1}{x}} - 1}.$$ (3.2)

Curve fitting was performed using the standard Levenberg-Marquardt algorithm with a, v_0, Δv, x, and the coefficients of $b(v)$ as free parameters. Experimentally the lines were found to be more sharply peaked than a pure Lorentzian, perhaps because the optical thickness of the discharge column accentuated the narrowness of the absorption feature. In order to mimic the line shapes, the first term in Equation (3.1) was chosen as a Lorentzian raised to the x power, where x was generally found in the range 1.5–3.5. Since it preserves the symmetry of the peak function, the inclusion of the exponent x

Figure 3.1. Trace of the ^{4}He $2^3S_1-2^3P_0$ transition and the corresponding fit. The cell pressure was 50 mTorr and the discharge supply voltage was 280 V. The middle graph shows the fit residuals while the top graph displays the sweep-laser pump power across the scan. The frequency was measured, as always, with respect to the clock laser.
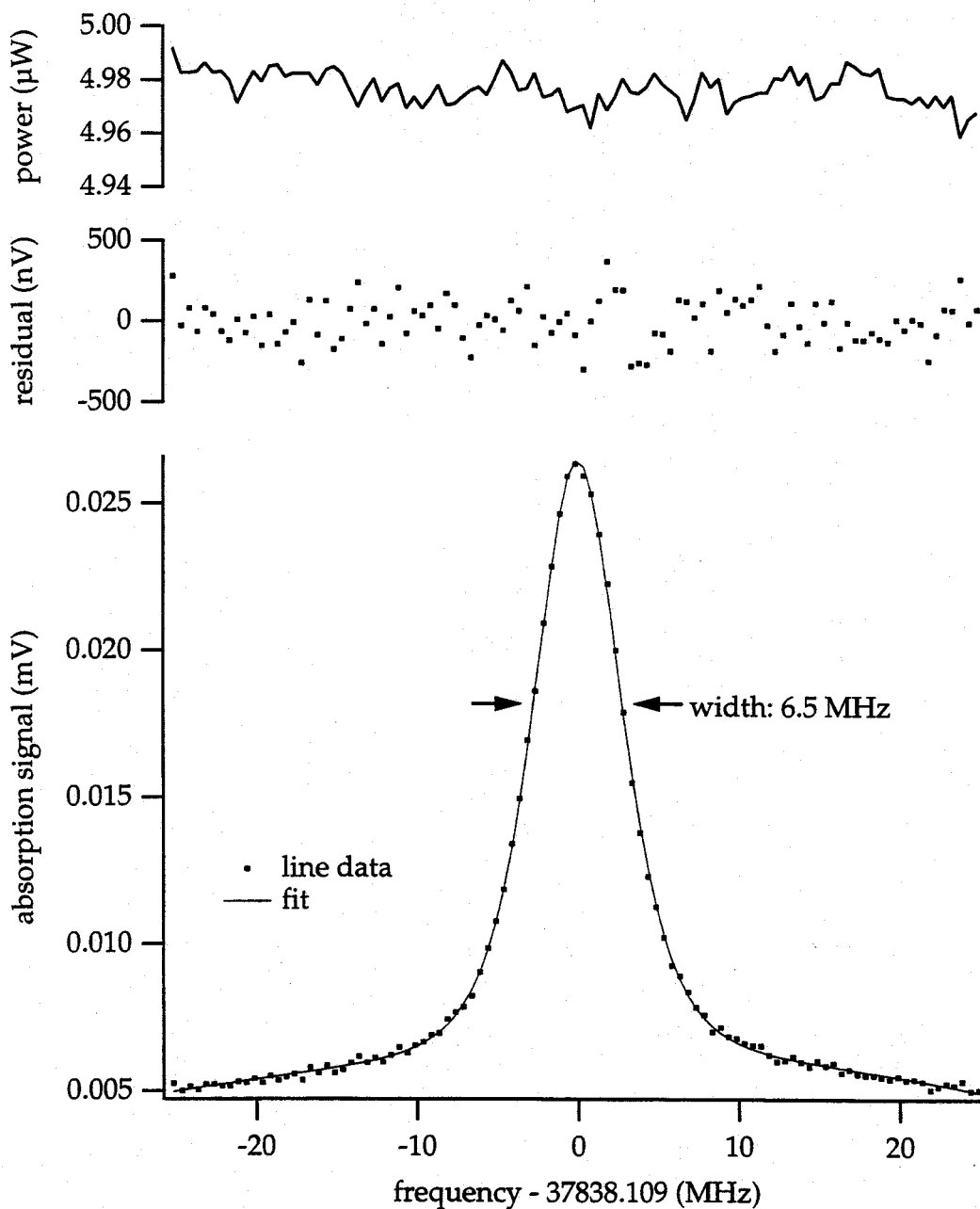
Figure 3.2. Trace of the ^{4}He $2^3S_1-2^3P_0$ transition and the corresponding fit. Except for lower sweep-laser power, the parameters, i.e., 50 mTorr and 280 V, are the same as in Figure 3.1. The middle graph shows the fit residuals while the top graph displays the sweep-laser pump power across the scan. The frequency was measured, as always, with respect to the clock laser.

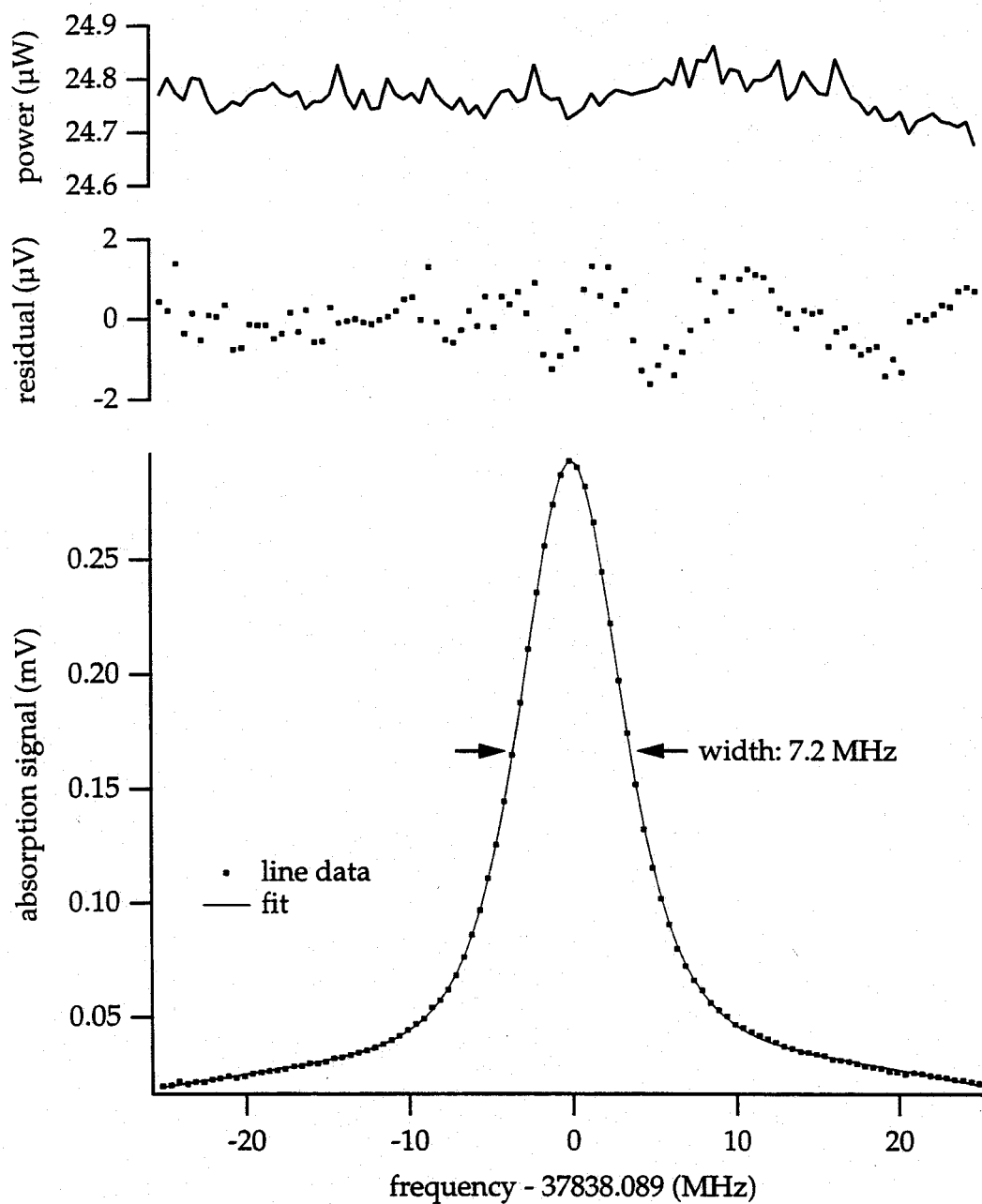**Figure 3.3.** Trace of the ^{4}He 2^3S_1–2^3P_0 transition and the corresponding fit. The cell pressure was 200 mTorr and the discharge supply voltage was 130 V. The middle graph shows the fit residuals while the top graph displays the sweep-laser pump power across the scan. The frequency was measured, as always, with respect to the clock laser.
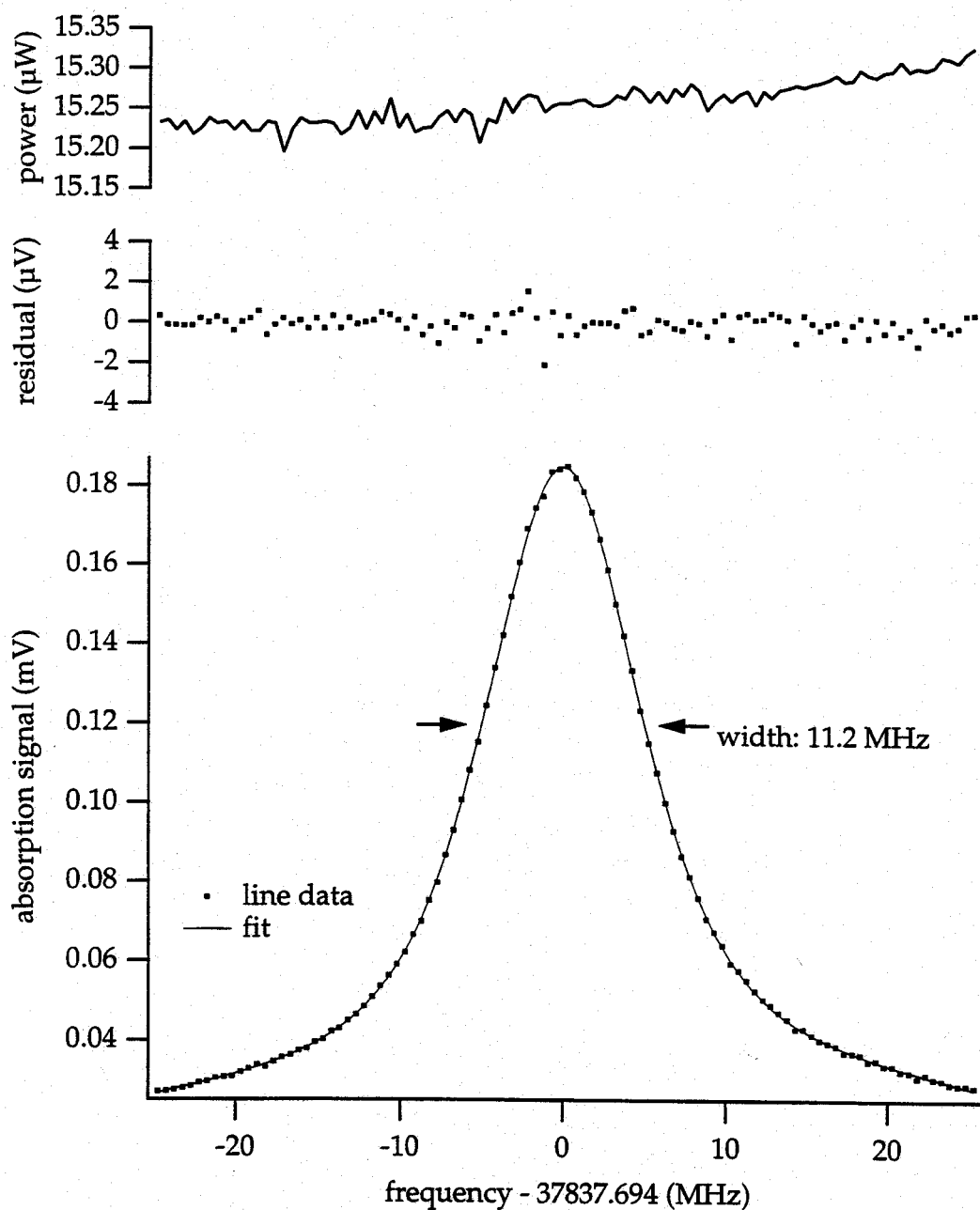
should not alter the line center produced by the fit. However, the choice of $b(v)$ may affect the line center and this issue is investigated later in this section. The middle part of Figures 3.1–3.3 gives the residuals from the fit while the top trace shows the variation in sweep laser power across the scan. Attempts to normalize the absorption signal against the laser power produced no improvement in the quality of the data and thus no power normalization is included in the present analysis.

Although the line centers are the primary concern, it is perhaps worthwhile to make a few remarks on the amplitude and width of the lines. The contrast between scans taken at different sweep laser powers can be seen by comparing Figure 3.1, obtained with 25 μW of pump, and Figure 3.2, produced using 5 μW. The higher power results in a marked increase in peak amplitude and signal-to-noise ratio while producing little change in line width thus implying that power broadening is not a significant effect at the intensities employed here. However, comparison of Figures 3.1 and 3.2, taken at a cell pressure of 50 mTorr, with Figure 3.3, taken at 200 mTorr, reveals an increased line width as the result of pressure broadening. Varying the discharge strength produced no appreciable change in line width thus leaving cell pressure as the main determinant of the width. In summary, the pressure-dependent widths for all three transitions are: 6.5 MHz at 50 mTorr, 10.8 MHz at 100 mTorr, and 11.2 MHz at 200 mTorr. A quantitative explanation of these results must await a better understanding of the various mechanisms in the discharge.

In addition to being dependent on the incident laser power, the absorption signal strength is, of course, also determined by the density of metastable helium atoms. Initially, at low metastable densities, the amplitude of each line increases with the metastable population, which, in-

this case, is controlled by cell pressure and discharge intensity. Figure 3.4, taken at 50 mTorr, shows the peak height of each line increasing with the discharge voltage. However, as the number of metastables is made to rise even further, the degree of absorption becomes so great that the pump and probe beams, entering from opposite sides of the discharge column, are substantially attenuated before they can interact thereby resulting in a reduction of the saturated-absorption signal. The observed amplitude from each transition is thus maximized at some metastable density. This "optimum" density would be higher for lines with weaker atomic oscillator strengths. The effect can be observed in the higher pressure 200 mTorr cell and is depicted in Figure 3.5, which shows the 2^3S_1–2^3P_1 and 2^3S_1–2^3P_2 line amplitudes reaching their respective maxima as functions of discharge voltage. The 2^3S_1–2^3P_2 transition, being the strongest of the three, has its maximum at the lowest discharge level while the 2^3S_1–2^3P_0 transition, being the weakest, has yet to reach its maximum even at the upper end of the discharge supply voltage range. Although it is easy to infer the relative order of the oscillator strengths of the three lines from Figures 3.4 and 3.5, a careful quantitative determination would require a more detailed knowledge of the discharge.

Line centers obtained at 50 mTorr over a range of discharge supply voltages are plotted in Figure 3.6 for all three transitions. A similar graph for the 200 mTorr cell is given in Figure 3.7. The data for each pressure were all taken in one session and, to insure a good signal-to-noise ratio, the laser power was fixed at a reasonably high value between 10 μW and 25 μW for each combination of cell pressure and helium transition. The repeated data points, seen at 280 V in the 50 mTorr graph and 150 V in the 200 mTorr graph, result from the first and last scans taken for each transition and give an
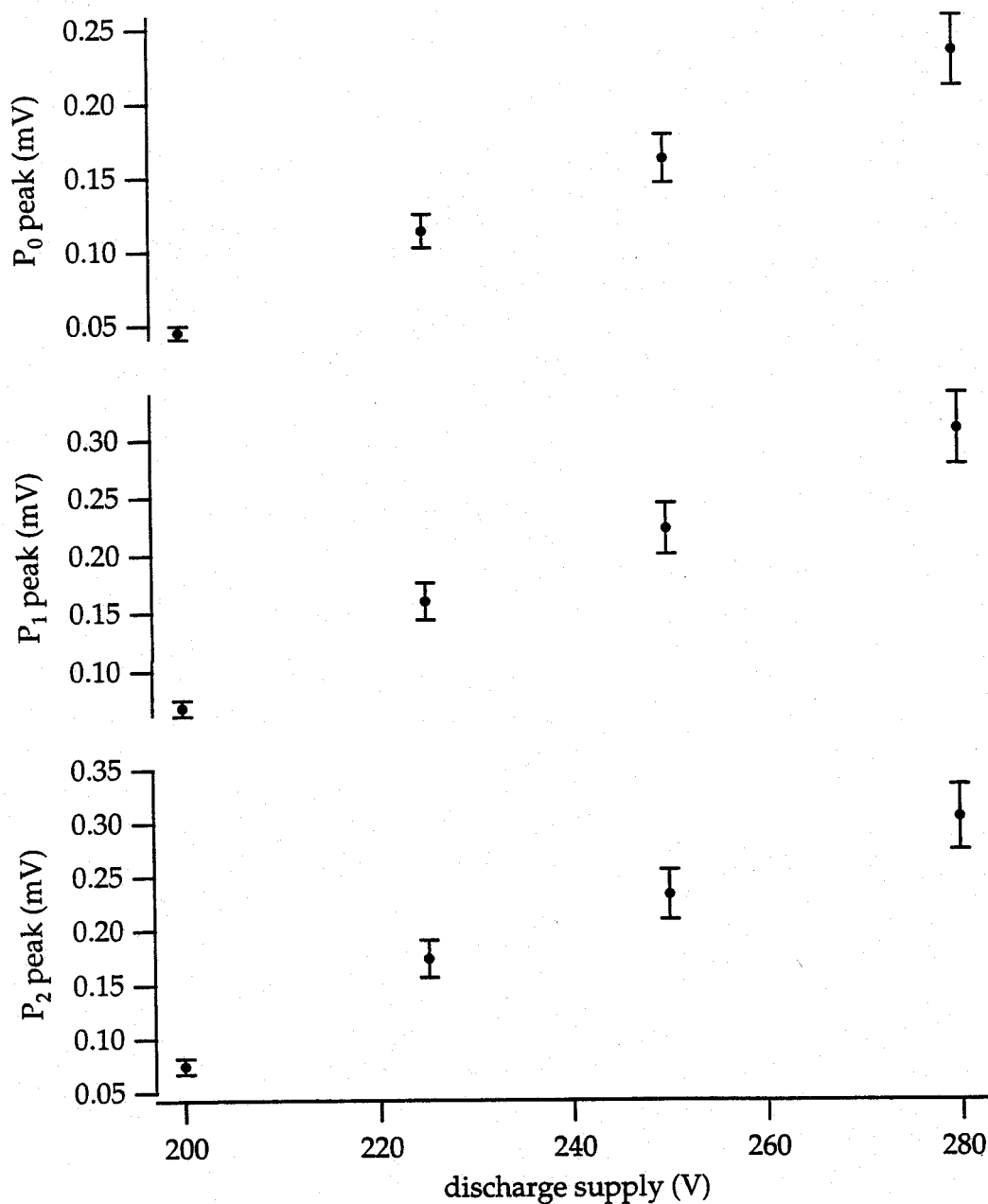
Figure 3.4. Amplitude of the saturated-absorption peak as a function of discharge strength for each transition at 50 mTorr. The sweep-laser pump power was fixed at 24 µW for the top graph and 14 µW for the middle and bottom graphs. The error bars indicate the observed reproducibility.
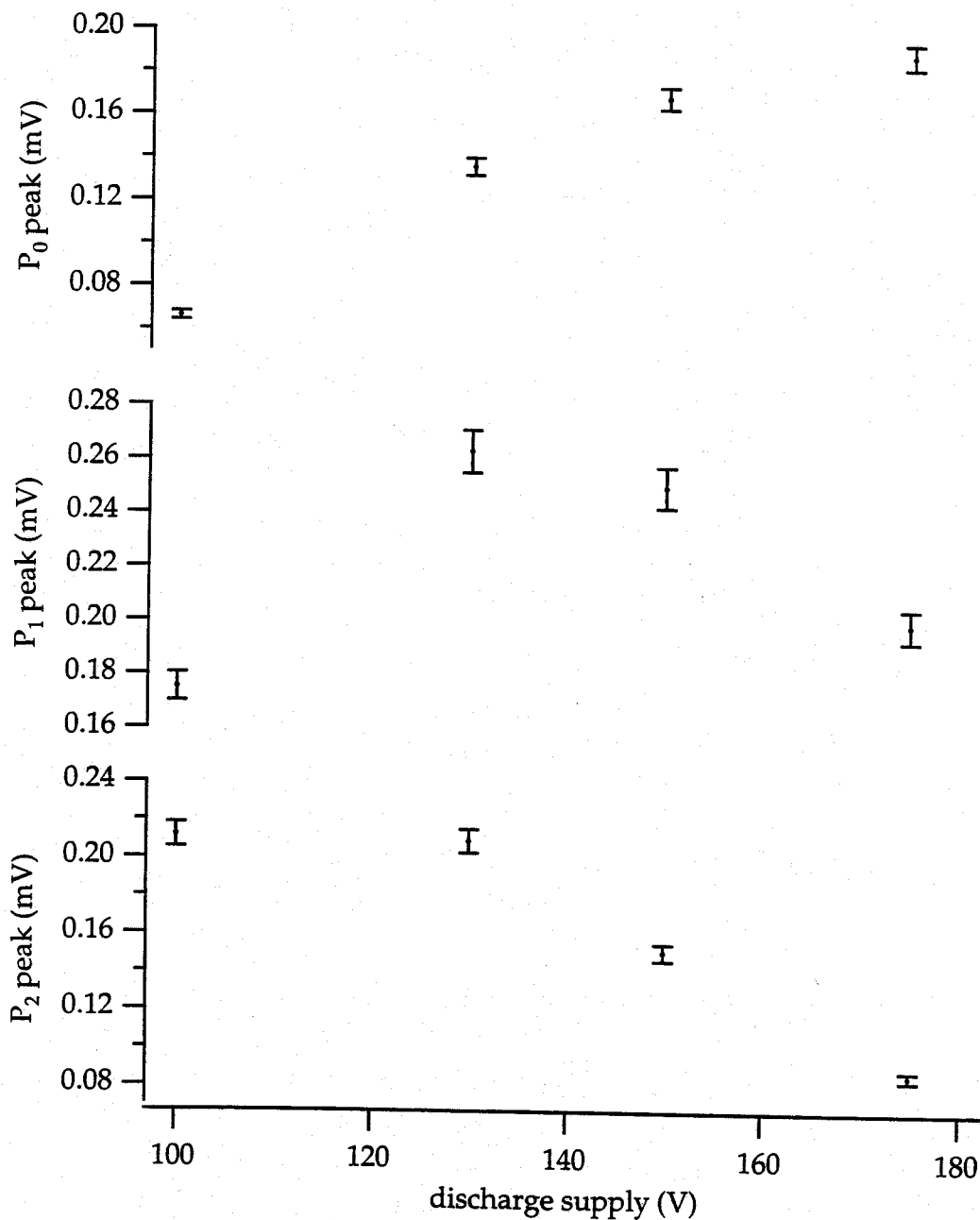
Figure 3.5. Amplitude of the saturated-absorption peak as a function of discharge strength for each transition at 200 mTorr. The sweep-laser pump power was fixed at 15 μW for all three graphs. The error bars indicate the observed reproducibility.

Figure 3.6. Line center as a function of discharge strength for each transition at 50 mTorr. The sweep-laser pump power was fixed at 24 μW for the top graph and 14 μW for the middle and bottom graphs. The error bars are assigned by the fit algorithm while the repeated points at 280 V reflect the observed reproducibility.
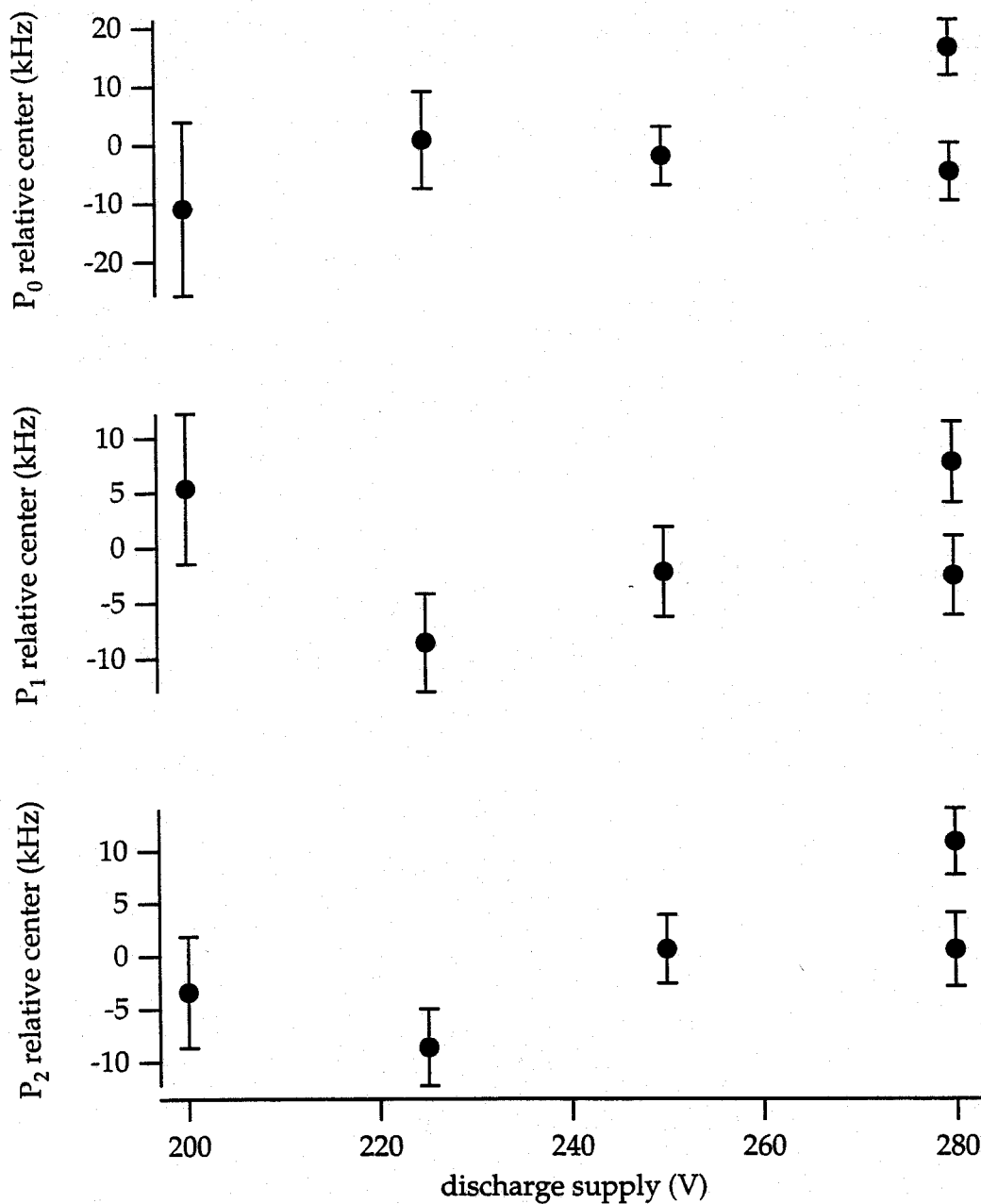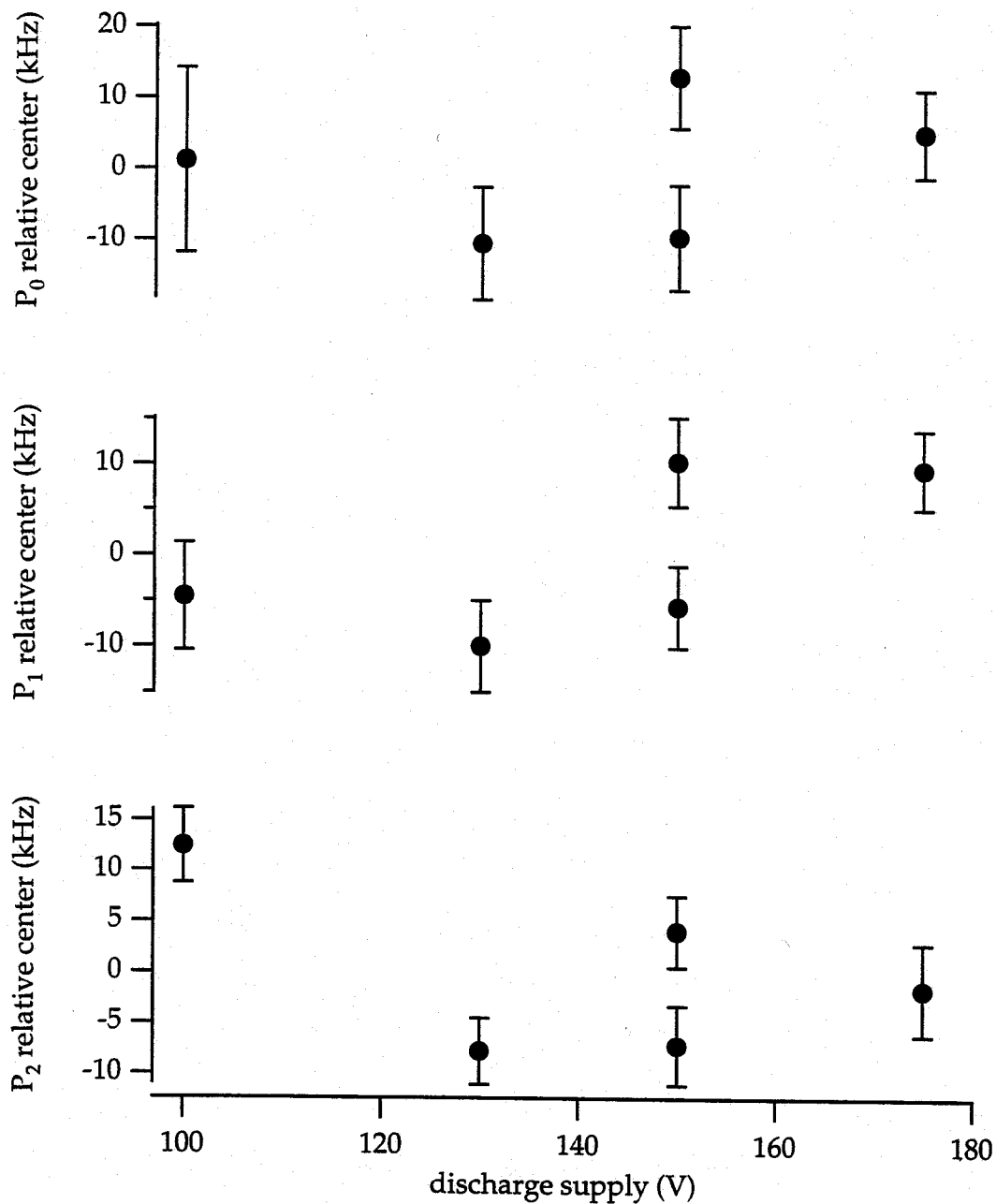
Figure 3.7. Line center as a function of discharge strength for each transition at 200 mTorr. The sweep-laser pump power was fixed at 15 μW for all three graphs. The error bars are assigned by the fit algorithm while the repeated points at 150 V reflect the observed reproducibility.

indication of the reproducibility of the measurements. At the current level of precision, there appears to be no discernible dependence of line center on discharge voltage.

Unfortunately, the situation is quite different with regard to line shifts related to laser power and cell pressure. It will be seen that increasing either power or pressure leads to a shift in the line center as well as a greater degree of asymmetry in the line shape. In addition to obtaining line centers over a range of laser powers, the symmetry of the lines was checked by varying the weight coefficients of the fit and noting the effect on the center. Again, the fitting function is given by Equation (3.1) although in this instance the baseline $b(v)$ is constrained to be only a constant. The data points of each trace were fit once with equal weighting and once weighted as the reciprocal of their square root. The variation of the center between the two fits serves as a gauge of line symmetry since the center of a perfectly symmetric line is independent of weighting formula. It should be noted that the square-root weighting is employed here merely as a convenient means to emphasize different sections of the line and is unrelated to the noise or uncertainty of each point. In fact, at the low beam power incident on the cell, the photon shot noise is below the specified $2.5\,\mathrm{pW}/\sqrt{\mathrm{Hz}}$ minimum noise equivalent power of the photoreceiver so the square-root weighting is unlikely to have any physical basis.

The line centers resulting from each type of weighting are plotted against pump power for all three transitions at 50 mTorr in Figure 3.8. The data points are repeated at each power with various intervening time intervals to give an indication of the scatter in the measurement. As can be seen, there is an overall shift toward lower frequencies at higher powers with the effect being more pronounced in the case of equal weighting. Since the
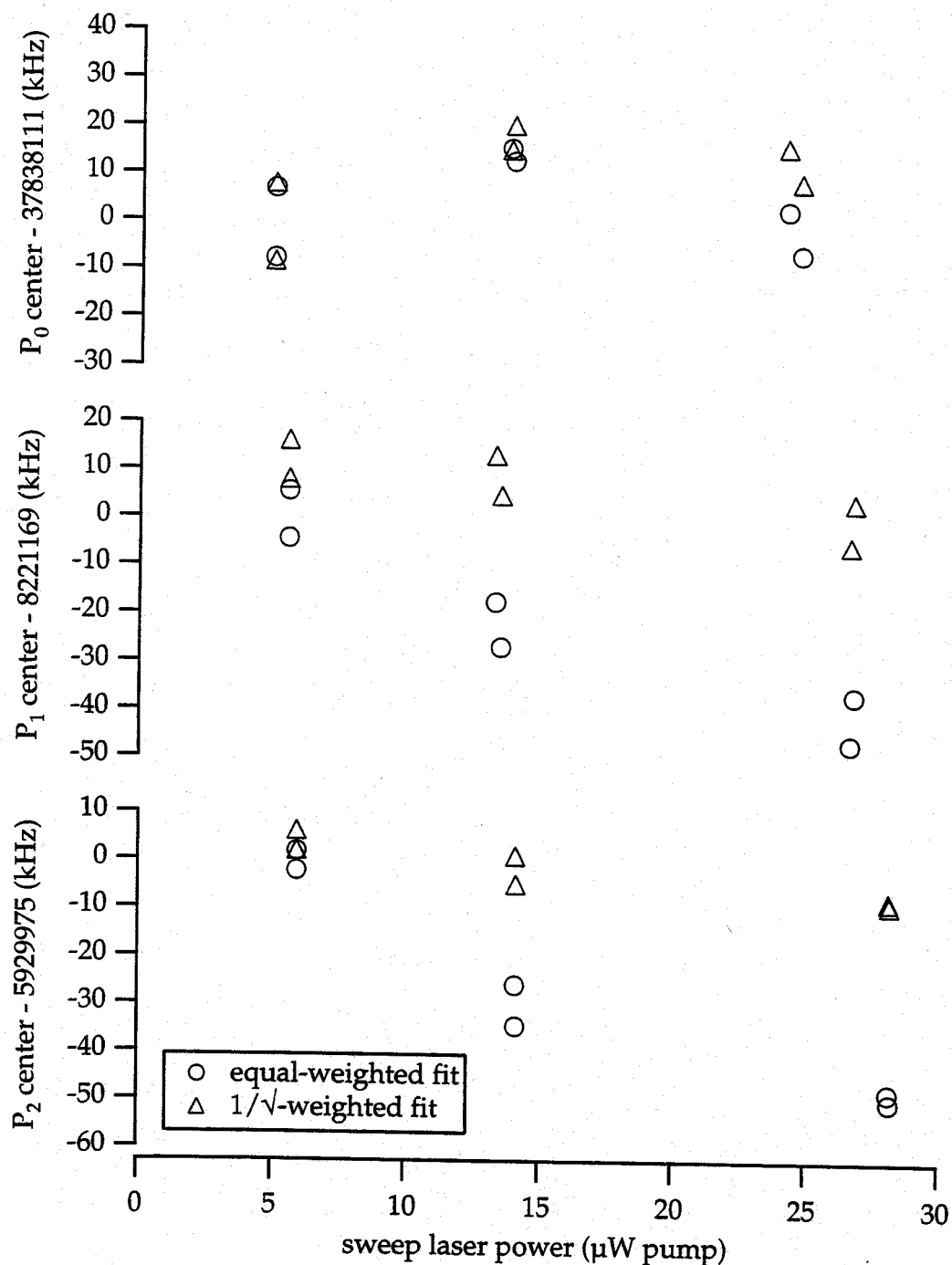
Figure 3.8. Line center as a function of sweep-laser pump power for the ^{4}He $2^3S_1-2^3P_{0,1,2}$ transitions at 50 mTorr. The discharge supply voltage was fixed at 280 V. Centers are shown from each type of fit weighting. The repeated points at each power give some indication of the observed reproducibility.

square-root weighting places more emphasis on points farther from the peak, greater power apparently gives rise to an asymmetry in the line shape characterized by elevation of the high-frequency shoulder thereby causing the square-root weighting to give a higher center. Indeed, careful examination of line scans reveals the presence of such an asymmetry, which is also reflected in the residual plot of Figure 3.1.

As shown in Figure 3.8, the centers obtained with different weighting choices approach each other with decreasing power. At the lowest-power point for each transition at 50 mTorr, agreement between the two types of weighting seems to indicate that the power shift of the center has been reduced to a level below or at least comparable to the measurement scatter from, *e.g.*, frequency drift in the clock laser. An identical analysis was undertaken for the line traces from the 100 and 200 mTorr cells and the average of the two centers at the lowest power is given in the first two columns of Table 3.1 for each transition, pressure, and form of weighting. Aside from an offset added to all the 100 mTorr 2^3S_1–2^3P_0 centers to correct for an abrupt change in clock-laser frequency, no other correction was applied to this table. Although all three cells display the same type of line shift and asymmetry, the agreement between the equal- and square-root-weighted results becomes increasingly worse with higher pressure thus suggesting an asymmetry related to pressure as well as power. Attempts to acquire data with pump powers much below 5 μW yielded unacceptably poor signal-to-noise ratios. The source of the power and pressure dependence in the lines has yet to be determined but a possible avenue for investigation is discussed in Chapter 4.

The third column of Table 3.1 gives centers generated from an equal-weighted fit with the baseline $b(v)$ taken as a polynomial containing terms up

P_0 center (in MHz) at lowest-power point

pressure (mTorr)	Lorentzian^x equal weighted	Lorentzian^x 1/√ weighted	Lorentzian^x + cubic
50	37838.111	37838.111	37838.103
100	37837.933	37837.953	37837.897
200	37837.723	37837.755	37837.658

P_1 center (in MHz) at lowest-power point

pressure (mTorr)	Lorentzian^x equal weighted	Lorentzian^x 1/√ weighted	Lorentzian^x + cubic
50	8221.169	8221.181	8221.153
100	8220.992	8221.020	8220.946
200	8220.844	8220.891	8220.752

P_2 center (in MHz) at lowest-power point

pressure (mTorr)	Lorentzian^x equal weighted	Lorentzian^x 1/√ weighted	Lorentzian^x + cubic
50	5929.975	5929.979	5929.964
100	5929.788	5929.805	5929.756
200	5929.547	5929.573	5929.505

Table 3.1. Average of the two line centers at the lowest laser power for all three transitions. Each column results from a different type of fit.

to third order. Comparison against the values in the first column, which were produced under the assumption of a constant baseline, reveals a shift in the opposite direction from that produced by the square-root weighting. This is to be expected since with the cubic baseline the line asymmetry is being subtracted by the fit as opposed to weighted. Of course both the square-root-weighting and cubic-baseline approaches to extracting line centers are rather extreme artificial devices introduced to gauge the range of possible outcomes. As an additional illustration of the reproducibility within the data, the separations between line centers obtained under presumably identical conditions were tabulated and a histogram of the number of occurrences of each value is given in Figure 3.9.

By subtracting corresponding entries in Table 3.1, values of the fine-structure intervals, given in Table 3.2, are obtained for the various pressures, *etc.* The final measurement result for each interval is taken to be the average of the constant-baseline equal- and square-root-weighted values at the lowest pressure (50 mTorr) and power. The square-root-weighted intervals are included to compensate for the general shift toward higher frequency with decreasing power evident in the 2^3S_1–2^3P_1 and 2^3S_1–2^3P_2 transition centers plotted in Figure 3.8. Furthermore, the 100 mTorr intervals are reasonably close to those at 50 mTorr and provide some assurance that pressure-dependent effects have subsided at 50 mTorr. However, the 200 mTorr entries clearly retain large unquantified systematic shifts and are excluded from consideration.

The admittedly crude correction for the power-dependence of the line centers and the absence of a reliable physical model require the assignment of an uncertainty sufficient to encompass both types of weighting. From the 12 kHz maximum deviation seen in Table 3.2 between the two weighting
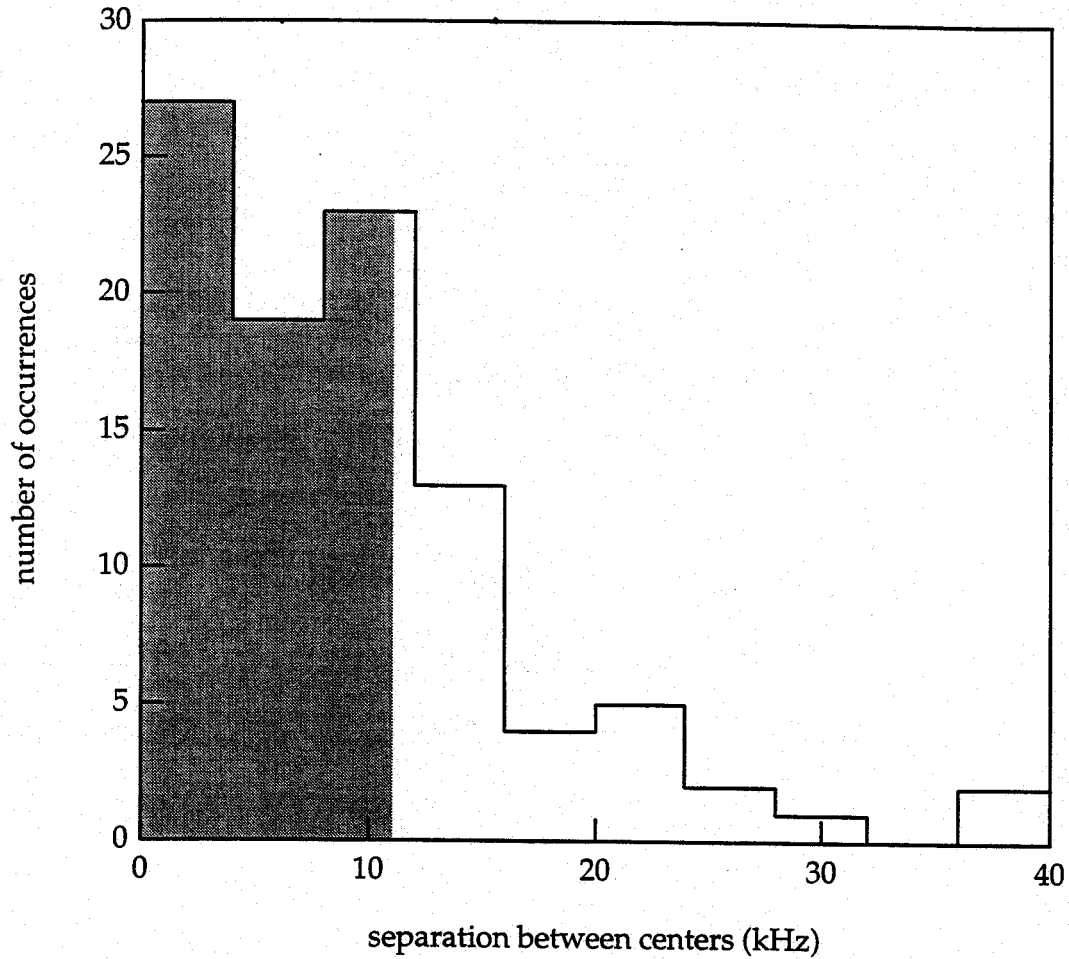
Figure 3.9. Histogram of the separations between line centers taken under presumably identical conditions. The shaded region contains 68% of the data.

methods, the uncertainty due to the power correction is taken to be ± 6 kHz. The diminished line asymmetry at the lowest pressure and power probably indicates that the center will not continue to shift with an additional decrease in power. This certainly appears to be the case for the weak 2^3S_1–2^3P_0 transition where the power shift and line asymmetry abruptly decrease in unison. In any event, even a smoother extrapolation of the 2^3S_1–$2^3P_{1,2}$ centers would only result in a further correction of order 6 kHz. From the

P_0–P_1 interval (in MHz) at lowest-power point

pressure (mTorr)	Lorentzian^x equal weighted	Lorentzian^x $1/\sqrt{}$ weighted	Lorentzian^x + cubic
50	29616.942	29616.930	29616.950
100	29616.941	29616.933	29616.951
200	29616.879	29616.864	29616.906

P_0–P_2 interval (in MHz) at lowest-power point

pressure (mTorr)	Lorentzian^x equal weighted	Lorentzian^x $1/\sqrt{}$ weighted	Lorentzian^x + cubic
50	31908.136	31908.132	31908.139
100	31908.145	31908.148	31908.141
200	31908.176	31908.182	31908.153

P_1–P_2 interval (in MHz) at lowest-power point

pressure (mTorr)	Lorentzian^x equal weighted	Lorentzian^x $1/\sqrt{}$ weighted	Lorentzian^x + cubic
50	2291.194	2291.202	2291.189
100	2291.204	2291.215	2291.190
200	2291.297	2291.318	2291.247

Table 3.2. The fine-structure intervals obtained by subtracting corresponding entries from Table 3.1.

data shown in Figure 3.9, it is found that 68% of the repeated centers are separated by 11 kHz or less. The uncertainty due to reproducibility is thus assigned to be ± 5.5 kHz. Adding this value in quadrature with the power-correction uncertainty gives a total uncertainty of 8 kHz. Table 3.3 summarizes the final results.

For completeness, it should be noted that corrections due solely to light shifts and external fields are completely negligible at the present level of precision. For the low beam intensities employed here, the light shifts should not exceed those of order 100 Hz observed [38, 39] in optical pumping of ^{3}He. Based on previous [20-22] calculations and measurements of the Zeeman effect for the 2^3P states, the upper limit of 50 mG established for the magnetic field in the vicinity of the cells gives shifts for the fine-structure splittings of less than a few Hz. Similarly, the calculated [1] Stark shift in the 2^3P terms amounts to less than a Hz for electric fields up to a few V/cm.

^{4}He fine-structure interval	result
2^3P_0–2^3P_1	29616.936(8)
2^3P_0–2^3P_2	31908.134(8)
2^3P_1–2^3P_2	2291.198(8)

Table 3.3. Final measurement results (in MHz).

References

[1] Hans A. Bethe and Edwin E. Salpeter, *Quantum Mechanics of One- and Two-Electron Atoms* (Plenum, New York, 1977).

[2] Barry N. Taylor, in *Units and Fundamental Constants in Physics and Chemistry*, Landolt-Börnstein Numerical Data and Functional Relationships in Science and Technology, edited by J. Bortfeldt and B. Kramer (Springer-Verlag, Berlin, 1995), p. 3-125-31.

[3] Robert S. Van Dyck Jr., Paul B. Schwinberg, and Hans G. Dehmelt, Phys. Rev. Lett. **59**, 26-9 (1987).

[4] T. Kinoshita, *Quantum Electrodynamics* (World Scientific, Singapore, 1990).

[5] E. Kruger, W. Nistler, and W. Weirauch, Metrologia **32**, 117-28 (1995).

[6] E. W. Hagley and F. M. Pipkin, Phys. Rev. Lett. **72**, 1172-5 (1994).

[7] Zong-Chao Yan and G. W. F. Drake, Phys. Rev. Lett. **74**, 4791-4 (1995).

[8] Barry N. Taylor and E. Richard Cohen, Phys. Lett. A **153**, 308-12 (1991).

[9] Marvin Douglas and Norman M. Kroll, Ann. Phys. (N.Y.) **82**, 89-155 (1974).

[10] James Daley, Marvin Douglas, Lars Hambro, and Norman M. Kroll, Phys. Rev. Lett. **29**, 12-5 (1972).

[11] Lars Hambro, Phys. Rev. A **5**, 2027-45 (1972).

[12] Michael L. Lewis and Paul H. Serafino, Phys. Rev. A **18**, 867-88 (1978).

[13] Tao Zhang and G. W. F. Drake, J. Phys. B **27**, L311-6 (1994).

[14] G. W. F. Drake (private communication).

[15] I. Wieder and W. E. Lamb, Phys. Rev. **107**, 125-34 (1957).

[16] J. Brochard, R. Chabbal, H. Chantrel, and P. Jacquinot, J. Phys. Radium **13**, 433-7 (1952).

[17] F. D. Colegrove, P. A. Franken, R. R. Lewis, and R. H. Sands, Phys. Rev. Lett. **3**, 420-2 (1959).

[18] W. Frieze, E. A. Hinds, V. W. Hughes, and F. M. J. Pichanick, Phys. Rev. A **24**, 279-87 (1981).

[19] A. Kponou, V. W. Hughes, C. E. Johnson, S. A. Lewis, and F. M. J. Pichanick, Phys. Rev. Lett. **26**, 1613-6 (1971).

[20] A. Kponou, V. W. Hughes, C. E. Johnson, S. A. Lewis, and F. M. J. Pichanick, Phys. Rev. A **24**, 264-78 (1981).

[21] S. A. Lewis, F. M. J. Pichanick, and V. W. Hughes, Phys. Rev. A **2**, 86-101 (1970).

[22] F. M. J. Pichanick, R. D. Swift, C. E. Johnson, and V. W. Hughes, Phys. Rev. **169**, 55-78 (1968).

[23] Laird D. Schearer, Michele Leduc, Daniel Vivien, Anne-Marie Lejus, and Jeanine Thery, IEEE J. Quantum Electron. **QE-22**, 713-7 (1986).

[24] Ping Zhao, J. R. Lawall, and F. M. Pipkin, Phys. Rev. Lett. **66**, 592-5 (1991).

[25] Ping Zhao, J. R. Lawall, A. W. Kam, M. D. Lindsay, F. M. Pipkin, and W. Lichten, Phys. Rev. Lett. **63**, 1593-6 (1989).

[26] D. Shiner, R. Dixson, and P. Zhao, Phys. Rev. Lett. **72**, 1802-5 (1994).

[27] R. Dixson and D. Shiner, Bull. Am. Phys. Soc. **39**, 1059 (1994).

[28] E. A. Hinds, J. D. Prestage, and F. M. J. Pichanick, Phys. Rev. A **32**, 2615-21 (1985).

[29] Ti Chuang and Harold J. Metcalf, Appl. Opt. **30**, 2495-502 (1991).

[30] T. Y. Fan and M. R. Kokta, IEEE J. Quantum Electron. **25**, 1845-9 (1989).

[31] Walter R. Leeb, Appl. Phys. **6**, 267-72 (1975).

[32] C. S. Adams, J. Vorberg, and J. Mlynek, Opt. Lett. **18**, 420-2 (1993).

[33] S. D. Rosner and F. M. Pipkin, Phys. Rev. A **1**, 571-86 (1970).

[34] John Russell Lawall, Ph.D. thesis (Harvard University, 1993).

[35] J. L. Hall, L. Holberg, T. Baer, and H. G. Robinson, Appl. Phys. Lett. **39**, 680-2 (1981).

[36] G. C. Bjorklund, M. D. Levenson, W. Lenth, and C. Ortiz, Appl. Phys. B **32**, 145-52 (1983).

[37] Edward A. Whittaker, Manfred Gehrtz, and Gary C. Bjorklund, J. Opt. Soc. Am. B **2**, 1320-6 (1985).

[38] L. D. Schearer, Phys. Rev. **127**, 512-7 (1962).

[39] L. D. Schearer and F. D. Sinclair, Phys. Rev. **175**, 36-9 (1968).

[40] F. S. Pavone (private communication).

[41] Dieter Hils and J. L. Hall, Rev. Sci. Instrum. **58**, 1406-12 (1987).

[42] Ch. Salomon, D. Hils, and J. L. Hall, J. Opt. Soc. Am. B **5**, 1576-87 (1988).

[43] P. W. Smith and T. Hänsch, Phys. Rev. Lett. **26**, 740-3 (1971).

Chapter 4
Conclusion

The results presented in Chapter 3 demonstrate the reliability of the experiment at the 8 kHz level. The present measurement is thus accurate enough to permit meaningful comparison with all previous values from theory and experiment. Table 4.1 shows the fine-structure splittings obtained from theory as well as from experiments claiming an uncertainty at or below a few ppm. The same information is presented graphically in Figure 4.1. With the calculation of terms of order α^5 and $\alpha^4 \mu / M$ still to be completed, the uncertainty for the theory is probably around 20 kHz [14]. The shaded regions in Figure 4.1 span intervals of ± 20 kHz about the latest theoretical values. It should be mentioned that yet another measurement of the ^{4}He 2^3P fine

^{4}He fine-structure interval	this work	Shiner et al. [26, 27]	Hughes et al. [18, 20-22]	theory [14]
$2^3P_0 - 2^3P_1$	29616.936(8)	29616.962(3)	29616.864(36)	29616.914(20)
$2^3P_0 - 2^3P_2$	31908.134(8)	31908.135(3)	31908.040(20)	31908.096(20)
$2^3P_1 - 2^3P_2$	2291.198(8)	2291.173(3)	2291.196(5)	2291.182(20)

Table 4.1. Comparison between the present work and other results. All values are in MHz.
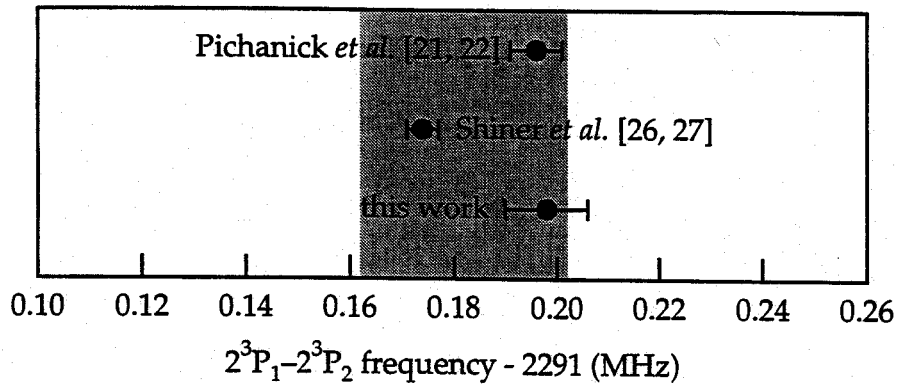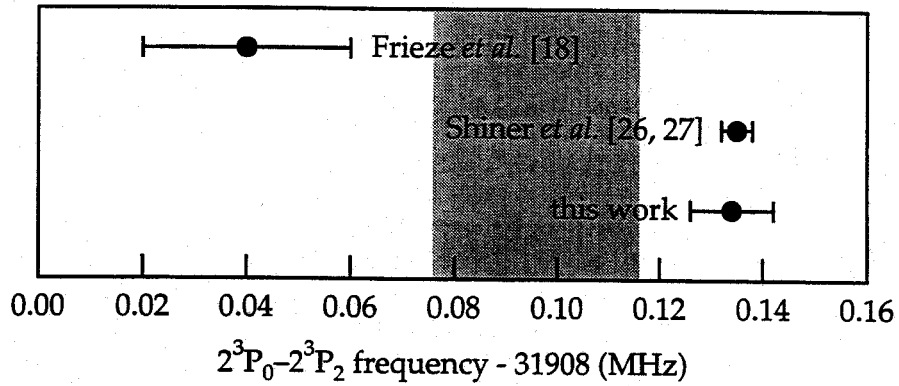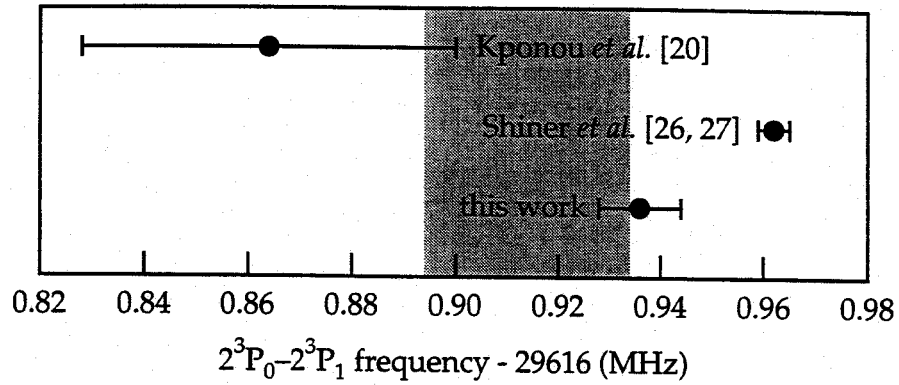
Figure 4.1. Graph of experimental and theoretical results for the 2^3P fine structure. The shaded regions span intervals of ± 20 kHz about the latest theoretical values [14].

structure is now underway at the European Laboratory for Non-Linear Spectroscopy in Firenze, Italy, and that a preliminary value of 29616.981(25) MHz for the 2^3P_0–2^3P_1 interval has been obtained [40]. Further investigations into this result appear to be ongoing and thus it has not been included in Table 4.1 and Figure 4.1.

There are a number of notable discrepancies between results from the present work and those of previous experiments. While this work agrees well with the microwave measurement of Hughes and coworkers for the small 2^3P_1–2^3P_2 interval, the present results for the 2^3P_0–2^3P_1 and 2^3P_0–2^3P_2 intervals are higher than obtained by Hughes *et al.*, by 2 and 4.7 respectively of the error bars of the latter. The present 2^3P_0–2^3P_2 value apparently corroborates the laser measurement of the interval by Shiner *et al.* However, differences of around 25 kHz persist between this experiment and that of Shiner *et al.* for the 2^3P_0–2^3P_1 and 2^3P_1–2^3P_2 splittings. Such disagreements are especially significant given the 3 kHz uncertainty claimed [27] by Shiner *et al.* The 9 kHz error bars initially assigned [26] by Shiner *et al.* would naturally make the discrepancies less pronounced but the values would still not quite be in agreement. Confirming measurements and further verification of error estimates seems desirable.

Since the uncertainty in the theory is due to uncalculated terms of order α^5 and $\alpha^4\mu/M$, a clean comparison with experiment must await the completion of these terms. The 20 kHz error bars quoted above from Drake were obtained by taking the largest term appearing in the now complete $\alpha^5\ln\alpha$ calculation and dividing it by $\ln\alpha$ to arrive at an estimate for the magnitude of the α^5 contribution. Since α^5 in atomic units corresponds to a frequency of about 140 kHz, the effect could in fact be larger depending on the constant multiplier for this order. Similarly, α^6 gives a factor of 1 kHz. Yan

and Drake have indicated [7] that the error bars in the theory will be reduced to ~0.5 kHz once calculations for terms of order α^5 and $\alpha^4 \mu/M$ are complete.

4.1 Future Directions

The accuracy of the experiment is presently limited by the reproducibility of the line centers and a dependence of the line symmetry and position on cell pressure and laser power. The variation among centers from repeated scans of a transition is probably attributable to drift in the frequency of the clock laser As discussed in Chapter 3, residual amplitude modulation (ram) in the eom is suspected as the cause of this drift. The effect might be greatly reduced by using third-order phase-modulation (pm) sidebands from the eom for fm spectroscopy instead of the first-order pm sidebands now employed for this purpose. It is expected that ram generates sidebands predominantly at the fundamental modulation frequency and its presence at the third harmonic should be extremely small. This technique has in fact been demonstrated [41, 42] for laser frequency locking though its efficacy in eliminating ram was not reported. The method appears to be very promising but proof of its effectiveness awaits implementation in the experiment.

The source of the pressure and power dependence in the lines is unclear. However, the asymmetry was observed always as an elevation of the high frequency shoulder of the line suggesting that some remnant of the Doppler profile, which also lies to the blue of the line, is being detected, perhaps via cross-relaxation effects [43]. If this were indeed the case, the saturated-absorption peak could be more closely centered on the Doppler profile by up-shifting with an aom the probe-beam frequency towards that of

the pump. The current 80 MHz pump-probe offset could be greatly reduced to be perhaps of order 100 kHz, which would still permit the elimination of spurious effects from optical interference as discussed in Chapter 3. Again, one can not be certain of the effectiveness of the scheme until it is demonstrated. Finally, replacement of the LNA lasers with recently available 1083 nm laser diodes (SDL-6702-H1) might be advantageous. Although not strictly necessary at this stage for improved accuracy, adoption of the diodes has the potential to make operation of the apparatus much simpler. It is hoped that with forthcoming progress the goal of a 10 ppb measurement, corresponding to an uncertainty of 300 Hz, will not prove too elusive.

References

[1] Hans A. Bethe and Edwin E. Salpeter, *Quantum Mechanics of One- and Two-Electron Atoms* (Plenum, New York, 1977).

[2] Barry N. Taylor, in *Units and Fundamental Constants in Physics and Chemistry*, Landolt-Börnstein Numerical Data and Functional Relationships in Science and Technology, edited by J. Bortfeldt and B. Kramer (Springer-Verlag, Berlin, 1995), p. 3-125-31.

[3] Robert S. Van Dyck Jr., Paul B. Schwinberg, and Hans G. Dehmelt, Phys. Rev. Lett. **59**, 26-9 (1987).

[4] T. Kinoshita, *Quantum Electrodynamics* (World Scientific, Singapore, 1990).

[5] E. Kruger, W. Nistler, and W. Weirauch, Metrologia **32**, 117-28 (1995).

[6] E. W. Hagley and F. M. Pipkin, Phys. Rev. Lett. **72**, 1172-5 (1994).

[7] Zong-Chao Yan and G. W. F. Drake, Phys. Rev. Lett. **74**, 4791-4 (1995).

[8] Barry N. Taylor and E. Richard Cohen, Phys. Lett. A **153**, 308-12 (1991).

[9] Marvin Douglas and Norman M. Kroll, Ann. Phys. (N.Y.) **82**, 89-155 (1974).

[10] James Daley, Marvin Douglas, Lars Hambro, and Norman M. Kroll, Phys. Rev. Lett. **29**, 12-5 (1972).

[11] Lars Hambro, Phys. Rev. A **5**, 2027-45 (1972).

[12] Michael L. Lewis and Paul H. Serafino, Phys. Rev. A **18**, 867-88 (1978).

[13] Tao Zhang and G. W. F. Drake, J. Phys. B **27**, L311-6 (1994).

[14] G. W. F. Drake (private communication).

[15] I. Wieder and W. E. Lamb, Phys. Rev. **107**, 125-34 (1957).

[16] J. Brochard, R. Chabbal, H. Chantrel, and P. Jacquinot, J. Phys. Radium **13**, 433-7 (1952).

[17] F. D. Colegrove, P. A. Franken, R. R. Lewis, and R. H. Sands, Phys. Rev. Lett. **3**, 420-2 (1959).

[18] W. Frieze, E. A. Hinds, V. W. Hughes, and F. M. J. Pichanick, Phys. Rev. A **24**, 279-87 (1981).

[19] A. Kponou, V. W. Hughes, C. E. Johnson, S. A. Lewis, and F. M. J. Pichanick, Phys. Rev. Lett. **26**, 1613-6 (1971).

[20] A. Kponou, V. W. Hughes, C. E. Johnson, S. A. Lewis, and F. M. J. Pichanick, Phys. Rev. A **24**, 264-78 (1981).

[21] S. A. Lewis, F. M. J. Pichanick, and V. W. Hughes, Phys. Rev. A **2**, 86-101 (1970).

[22] F. M. J. Pichanick, R. D. Swift, C. E. Johnson, and V. W. Hughes, Phys. Rev. **169**, 55-78 (1968).

[23] Laird D. Schearer, Michele Leduc, Daniel Vivien, Anne-Marie Lejus, and Jeanine Thery, IEEE J. Quantum Electron. **QE-22**, 713-7 (1986).

[24] Ping Zhao, J. R. Lawall, and F. M. Pipkin, Phys. Rev. Lett. **66**, 592-5 (1991).

[25] Ping Zhao, J. R. Lawall, A. W. Kam, M. D. Lindsay, F. M. Pipkin, and W. Lichten, Phys. Rev. Lett. **63**, 1593-6 (1989).

[26] D. Shiner, R. Dixson, and P. Zhao, Phys. Rev. Lett. **72**, 1802-5 (1994).

[27] R. Dixson and D. Shiner, Bull. Am. Phys. Soc. **39**, 1059 (1994).

[28] E. A. Hinds, J. D. Prestage, and F. M. J. Pichanick, Phys. Rev. A **32**, 2615-21 (1985).

[29] Ti Chuang and Harold J. Metcalf, Appl. Opt. **30**, 2495-502 (1991).

[30] T. Y. Fan and M. R. Kokta, IEEE J. Quantum Electron. **25**, 1845-9 (1989).

[31] Walter R. Leeb, Appl. Phys. **6**, 267-72 (1975).

[32] C. S. Adams, J. Vorberg, and J. Mlynek, Opt. Lett. **18**, 420-2 (1993).

[33] S. D. Rosner and F. M. Pipkin, Phys. Rev. A **1**, 571-86 (1970).

[34] John Russell Lawall, Ph.D. thesis (Harvard University, 1993).

[35] J. L. Hall, L. Holberg, T. Baer, and H. G. Robinson, Appl. Phys. Lett. **39**, 680-2 (1981).

[36] G. C. Bjorklund, M. D. Levenson, W. Lenth, and C. Ortiz, Appl. Phys. B **32**, 145-52 (1983).

[37] Edward A. Whittaker, Manfred Gehrtz, and Gary C. Bjorklund, J. Opt. Soc. Am. B **2**, 1320-6 (1985).

[38] L. D. Schearer, Phys. Rev. **127**, 512-7 (1962).

[39] L. D. Schearer and F. D. Sinclair, Phys. Rev. **175**, 36-9 (1968).

[40] F. S. Pavone (private communication).

[41] Dieter Hils and J. L. Hall, Rev. Sci. Instrum. **58**, 1406-12 (1987).

[42] Ch. Salomon, D. Hils, and J. L. Hall, J. Opt. Soc. Am. B **5**, 1576-87 (1988).

[43] P. W. Smith and T. Hänsch, Phys. Rev. Lett. **26**, 740-3 (1971).